Hadronic light-by-light contribution to the muon anomaly from lattice QCD with infinite volume QED at physical pion mass

Thomas Blum,[1,*] Norman Christ,[2] Masashi Hayakawa,[3,4] Taku Izubuchi,[5,6] Luchang Jin,[1,6,†] Chulwoo Jung,[5] Christoph Lehner,[7] and Cheng Tu[1]

(RBC and UKQCD Collaborations)

[1]*Physics Department, University of Connecticut, Storrs, Connecticut 06269-3046, USA*
[2]*Physics Department, Columbia University, New York, New York 10027, USA*
[3]*Department of Physics, Nagoya University, Nagoya 464-8602, Japan*
[4]*Nishina Center, RIKEN, Wako, Saitama 351-0198, Japan*
[5]*Physics Department, Brookhaven National Laboratory, Upton, New York 11973, USA*
[6]*RIKEN-BNL Research Center, Brookhaven National Laboratory, Upton, New York 11973, USA*
[7]*Fakultät für Physik, Universität Regensburg, Universitätsstraße 31, 93040 Regensburg, Germany*

(Received 22 May 2023; accepted 13 December 2024; published 10 January 2025)

The hadronic light-by-light scattering contribution to the muon anomalous magnetic moment, $(g-2)/2$, is computed in the infinite volume QED framework with lattice QCD. We report $a_\mu^{\mathrm{HLbL}} = 12.47(1.15)(0.95) \times 10^{-10}$ where the first error is statistical and the second systematic. The result is mainly based on the $2+1$ flavor Möbius domain wall fermion ensemble with inverse lattice spacing $a^{-1} = 1.73$ GeV, lattice size $L = 5.5$ fm, and $m_\pi = 139$ MeV, generated by the RBC-UKQCD collaborations. The leading systematic error of this result comes from the lattice discretization. This result is consistent with previous determinations.

DOI: 10.1103/PhysRevD.111.014501

I. INTRODUCTION

Muons are spin-1/2 charged particles with nonzero magnetic moment

$$\boldsymbol{\mu} = -g\frac{e}{2m}\mathbf{S}, \tag{1}$$

where $\mathbf{S}$ is the particle's spin, e and m are the electric charge and mass, respectively, and g is the Landé g-factor. The Dirac equation predicts that $g = 2$, exactly, so any difference from 2 must arise from interactions. The magnetic moment of a fermion can be defined in terms of its electromagnetic form factors in the zero momentum transfer limit. Lorentz and gauge symmetries tightly constrain the form of the interactions. In Euclidean space-time

$$\langle \mu(\mathbf{p}', s')|J_\nu(0)|\mu(\mathbf{p}, s)\rangle = -e\bar{u}_{s'}(\mathbf{p}')\left(F_1(q^2)\gamma_\nu + i\frac{F_2(q^2)}{4m}[\gamma_\nu, \gamma_\rho]q_\rho\right)u_s(\mathbf{p}), \tag{2}$$

where J_ν is the electromagnetic current, and F_1 and F_2 are form factors, giving the charge and magnetic moment at zero momentum transfer ($q^2 = (p'-p)^2 = 0$), or static limit. The $u_s(\mathbf{p})$ and $\bar{u}_s(\mathbf{p})$ are Dirac spinors. The anomalous part of the magnetic moment is given by $F_2(0)$ alone, and is known as the anomaly,

$$a_\mu \equiv F_2(q^2 = 0) = \frac{g-2}{2}. \tag{3}$$

The muon anomalous magnetic moment is one of the most precisely determined quantities in particle physics. Compared with the electron anomalous magnetic moment, which is determined with higher accuracy, the muon is expected to be much more sensitive to new physics at very large energy scales due to its heavier mass. Two experiments Fermilab (E989) [1] and J-PARC (E34) [2,3] are aiming at even higher precision in measuring the muon $g-2$. The initial result released by Fermilab (E989) [1] confirmed the previously best result obtained by the BNL E821 experiment [4] and reduced the experimental uncertainty from 0.54 to

*Contact author: thomas.blum@uconn.edu
†Contact author: ljin.luchang@gmail.com

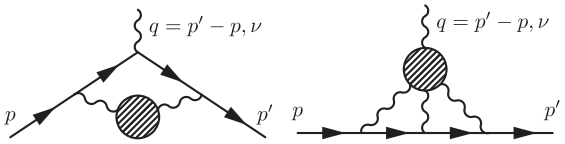

FIG. 1. The HVP (left) and HLbL (right) contribution to muon $g-2$. The shaded circles represent hadronic interactions.

0.46 ppm. The final goal of the Fermilab experiment is to reduce the uncertainty further to approximately 0.14 ppm. The J-PARC experiment adopts a very different measurement strategy and will serve as an important cross-check. Its final accuracy goal is 0.45 ppm for statistical uncertainty and 0.07 ppm for systematic uncertainty.

The Standard Model result provided by the muon $g-2$ theory initiative [5–25] currently has an uncertainty of 0.37 ppm and is in 4.2σ tension with the experimental value. The two leading sources of uncertainty come from the leading QCD contributions, hadronic vacuum polarization (HVP) and hadronic light-by-light (HLbL) scattering, both illustrated in Fig. 1.

For a long time, the HLbL contribution has been estimated by hadronic models [26–29]. In Refs. [30,31], the hadronic light-by-light scattering amplitudes estimated by hadronic models are compared with lattice QCD calculations. The result from hadronic models is difficult to improve further. More recently, the HLbL contribution has been calculated with the dispersion relation approach [17–25,32–37]. These results are summarized in the 2020 white paper [5],

$$a_\mu^{\mathrm{HLbL,WP2020,pheno}} \times 10^{10} = 9.2(1.9) \tag{4}$$

Within the dispersion relation framework, the pseudo-scalar pole is the leading contribution to HLbL. This contribution is defined in terms of the pseudo-scalar transition form factors to two (possibly off-shell) photons, $\pi^0, \eta, \eta' \to \gamma^*\gamma^*$. These form factors can also be calculated with lattice QCD. [21,38–40]

The first direct lattice QCD calculation of the HLbL contribution was performed by the RBC-UKQCD collaborations. [41] Then, we made many improvements to the calculation method and also included the contribution from the leading disconnected diagrams. [42,43] In our previous work [24], we applied the method developed to lattice gauge ensembles with different lattice spacings and spatial volumes, all at physical pion mass. The calculations incorporate both QCD and QED in the same finite volume lattice using the QED_L scheme [44]. We extrapolated the results to infinite volume and the continuum limit. The final result was

$$a_\mu^{\mathrm{HLbL,RBC\text{-}UKQCD2019}} \times 10^{10} = 7.87(3.06)_{\mathrm{stat}}(1.77)_{\mathrm{syst}}. \tag{5}$$

This was the first lattice QCD result for HLbL with all systematic effects controlled. The statistical error was still larger than the phenomenological results obtained with dispersion relations or the previous hadronic model estimation.

The Mainz group pioneered the QED_∞ approach and precalculated the QED kernel semianalytically in infinite volume [30,45]. We also explored this strategy and independently calculated the infinite volume QED weighting function [46]. In that work, we found that while the QED_∞ approach ensures an exponentially suppressed finite volume error, the size of the finite volume error can still be significant. However, making use of the current conservation property of the hadronic four point function, we designed subtractions to the infinite volume QED weighting functions to reduce the finite volume errors and also the discretization errors. The subtracted infinite volume QED weighting function is used in the current work.

The effectiveness of the subtraction is confirmed by the Mainz group and a different subtraction scheme was adopted in their calculation. [45,47–49]. Their calculation was performed with pion masses ranging from 200 to 420 MeV and extrapolated to the physical point. All subleading disconnected diagrams were carefully calculated and were found to be consistent with zero. The charm quark contribution from the connected and disconnected diagrams were calculated as well. Finally, a statistically more precise result was obtained

$$a_\mu^{\mathrm{HLbL,Mainz2021}} \times 10^{10} = 10.96(1.59). \tag{6}$$

In this work, we present our latest lattice calculation of the HLbL contribution to muon $g-2$ with subtracted infinite volume QED weighting function as developed in our previous work [46]. The calculation is directly performed at physical pion mass and therefore eliminates the systematic uncertainty from chiral extrapolations. We find that calculating the HLbL contribution directly at the physical pion mass is considerably more difficult than a calculation at a heavier pion mass due the larger contribution and statistical fluctuations from the long distance region. Following the suggestion of Ref. [48], we focus on the calculation of the connected and leading disconnected diagrams. The main calculation is performed with a single lattice spacing where $a^{-1} = 1.73$ GeV. While we use Möbius domain wall fermions (MDWF) to eliminate $\mathcal{O}(a)$ discretization errors, the remaining $\mathcal{O}(a^2)$ effects are estimated to be the largest source of systematic uncertainty of this calculation.

The paper is organized as follows: in Secs. II and III, we review the calculation method developed in our previous works and describe new techniques used in this calculation. We then show our numerical results in Sec. IV and conclude in Sec. V.

II. THEORETICAL FRAMEWORK AND CALCULATION METHOD

We base our current calculation on the framework already set up in our previous works [42,43,46]. In this work, we

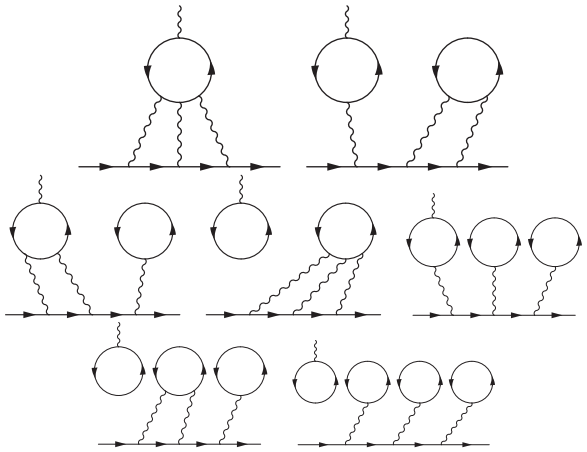

FIG. 2. Diagrams contributing to the muon anomaly. The diagrams in the top row are the leading ones, and do not vanish in the $SU(3)$ flavor limit. Strong interactions to all orders, including gluons connecting the quark loops and sea quark loops which are not connected by photons, are not shown.

combine the method used in Refs. [42,43] to calculate the hadronic four point function with lattice QCD with the subtracted infinite volume QED weighting function developed in Ref. [46]. We have tested the QED weighting function by calculating the leptonic light-by-light contribution to muon $g-2$ and have reproduced the results obtained by analytical calculation [50,51]. We outline the method below and focus on the improvements we made in this work.

All of the diagrams contributing at $O(\alpha^3)$ to HLbL scattering are shown in Fig. 2. We use the term (quark-) "connected diagram" to refer to the one on the left on the top row and "disconnected diagram" to refer to the one on the right. The remaining diagrams, which are all suppressed in the flavor SU(3) limit, are referred to as the "subleading disconnected diagrams." We only explicitly draw quark loops that are connected to photons. Gluons and sea quark loops that are not connected to photons are not shown in the figure but are included automatically in dynamical lattice QCD calculations. To make nonzero contributions to the muon $g-2$, the quark loops in the disconnected diagrams must be connected by gluons.

The contribution to the muon $g-2$ can be calculated with the combination of the hadronic four-point function $\mathcal{H}$ and the QED weighting function $\mathcal{G}$ [46]

$$a_\mu^{\mathrm{HLbL}} \frac{e}{m} \bar{u}_{s'}(\vec{0}) \frac{\Sigma_i}{2} u_s(\vec{0}) = \frac{1}{VT} \sum_{x_{\mathrm{op}}} \sum_{x,y,z} \frac{1}{2} \epsilon_{i,j,k} (x_{\mathrm{op}} - x_{\mathrm{ref}}(x,y,z))_j \times i^3 e^6 \mathcal{H}_{k,\rho,\sigma,\lambda}(x_{\mathrm{op}},x,y,z) \bar{u}_{s'}(\vec{0}) \mathcal{G}_{\rho,\sigma,\lambda}(x,y,z) u_s(\vec{0}), \quad (7)$$

where $\bar{u}_{s'}(\vec{0})$, $u_s(\vec{0})$ are Dirac spinors for the outgoing and incoming muon in the diagram, respectively. V stand for the spatial volume of the lattice and T stand for the size of the temporal extent of the lattice. $\Sigma_k = \epsilon_{i,j,k}\gamma_i\gamma_j/(2i)$ is the 4×4 version of the Pauli matrix, σ_k. From the spin structure of the muon particle, we can obtain the expression for a_μ^{HLbL}

$$a_\mu^{\mathrm{HLbL}} = \frac{2me^2}{3} \frac{1}{VT} \sum_{x_{\mathrm{op}}} \sum_{x,y,z} \frac{1}{2} \epsilon_{i,j,k} (x_{\mathrm{op}} - x_{\mathrm{ref}}(x,y,z))_j \times (6e^4) \mathcal{H}_{k,\rho,\sigma,\lambda}(x_{\mathrm{op}},x,y,z) \mathcal{M}_{i,\rho,\sigma,\lambda}(x,y,z) \quad (8)$$

where

$$\mathcal{M}_{i,\rho,\sigma,\lambda}(x,y,z) = \frac{1}{2} \mathrm{Tr}\left[\frac{1}{6} i^3 \mathcal{G}_{\rho,\sigma,\lambda}(x,y,z) \Sigma_i \right]. \quad (9)$$

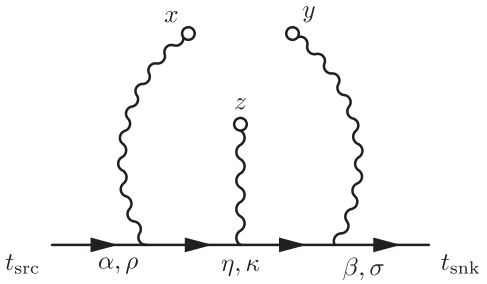

FIG. 3. Diagrammatic representation of the QED weighting function defined in Eq. (9), following Ref. [46].

The QED weighting function $\mathcal{G}$ is shown diagrammatically in Fig. 3 and is expressed in terms of the free muon and Feynman gauge photon propagators, S_μ and G

$$\mathfrak{G}_{\sigma,\kappa,\rho}(y,z,x) = \lim_{t_{\mathrm{src}}\to-\infty, t_{\mathrm{snk}}\to\infty} e^{m_\mu(t_{\mathrm{snk}}-t_{\mathrm{src}})} \times \int_{\alpha,\beta,\eta,\vec{x}_{\mathrm{snk}},\vec{x}_{\mathrm{src}}} G(x,\alpha) G(y,\beta) G(z,\eta) \times S_\mu(x_{\mathrm{snk}},\beta) i\gamma_\sigma S_\mu(\beta,\eta) i\gamma_\kappa S_\mu(\eta,\alpha) i\gamma_\rho \times S_\mu(\alpha,x_{\mathrm{src}}). \quad (10)$$

As is well known, the above expression contains an infrared divergence that vanishes after projection to its magnetic part. We can also remove this infrared divergent piece by the following procedure:

$$\mathfrak{G}^{(1)}_{\sigma,\kappa,\rho}(y,z,x) = \frac{1}{2}\mathfrak{G}_{\sigma,\kappa,\rho}(y,z,x) + \frac{1}{2}[\mathfrak{G}_{\rho,\kappa,\sigma}(x,z,y)]^\dagger. \quad (11)$$

In addition we can perform somewhat arbitrary subtractions to this infinite volume QED weighting function without changing the final result due to vector current conservation satisfied by the hadronic four point function,

$$\mathfrak{G}^{(2)}_{\sigma,\kappa,\rho}(y,z,x) = \mathfrak{G}^{(1)}_{\sigma,\kappa,\rho}(y,z,x) - \mathfrak{G}^{(1)}_{\sigma,\kappa,\rho}(z,z,x) - \mathfrak{G}^{(1)}_{\sigma,\kappa,\rho}(y,z,z). \quad (12)$$

Note that $\mathfrak{G}^{(1)}_{\sigma,\kappa,\rho}(z,z,z)=0$, so this subtraction significantly reduces the size of the QED weighting function when $|x-z|$ or $|y-z|$ is small. This is the region where the hadronic function from the lattice calculation has the largest discretization error. It turns out that this subtraction greatly reduces the discretization error. This is the major finding of Ref. [46]. We should also note that the subtraction does impact the integrand and partial sum. In Ref. [48], a modified subtraction scheme is used, so their integrand and partial sum cannot be directly compared with ours. Finally, we include all possible permutations of the subtracted QED weighting function which are required for the total contribution to the muon $g-2$:

$$\begin{aligned} i^3\mathcal{G}_{\rho,\sigma,\kappa}(x,y,z) &= \mathfrak{G}^{(2)}_{\rho,\sigma,\kappa}(x,y,z)+\mathfrak{G}^{(2)}_{\sigma,\kappa,\rho}(y,z,x) \\ &\quad+\mathfrak{G}^{(2)}_{\kappa,\rho,\sigma}(z,x,y)+\mathfrak{G}^{(2)}_{\kappa,\sigma,\rho}(z,y,x) \\ &\quad+\mathfrak{G}^{(2)}_{\rho,\kappa,\sigma}(x,z,y)+\mathfrak{G}^{(2)}_{\sigma,\rho,\kappa}(y,x,z). \end{aligned} \tag{13}$$

Another component of the master formula Eq. (8) is x_{ref}, the reference position for the moment method to calculate the magnetic moment. Again, due to current conservation, there are many possible choices for x_{ref}. In this work, we use the following choice for the connected diagram:

$$\begin{aligned} &x_{\mathrm{ref}}(x,y,z) \\ &= x_{\mathrm{ref-far}}(x,y,z) \\ &= \begin{cases} x & \text{if } |y-z| < \min(|x-y|,|x-z|) \\ y & \text{if } |x-z| < \min(|x-y|,|y-z|) \\ z & \text{if } |x-y| < \min(|x-z|,|y-z|) \\ \frac{1}{3}(x+y+z) & \text{otherwise} \end{cases} \end{aligned} \tag{14}$$

We make a slightly different choice of x_{ref}, Eq. (21), for the disconnected diagrams. The rationale will be described in the later part of this section. We use $\mathcal{H}$ to denote the hadronic four point function

$$(6e^4)\mathcal{H}_{k,\rho,\sigma,\lambda}(x_{\mathrm{op}},x,y,z)=\langle TJ_k(x_{\mathrm{op}})J_\rho(x)J_\sigma(y)J_\lambda(z)\rangle_{\mathrm{QCD}} \tag{15}$$

$$J_\nu(x)=\sum_{q=u,d,s,c} e_q Z_V \bar{\psi}_q(x)\gamma_\nu\psi_q(x) \tag{16}$$

where Z_V is the lattice local vector current renormalization constant. After Wick contraction, $\mathcal{H}$ can be expressed as the sum of different types of diagrams as illustrated in Fig. 2. For the disconnected and subleading disconnected diagrams, we require the quark loops to be connected by gluons.

$$\mathcal{H}=\mathcal{H}^{\mathrm{con}}+\mathcal{H}^{\mathrm{discon}}+\mathcal{H}^{\mathrm{subleading\text{-}discon}}+\mathcal{H}^{\mathrm{charm}} \tag{17}$$

where $\mathcal{H}^{\mathrm{con}}$ includes the light and strange quark connected diagrams, $\mathcal{H}^{\mathrm{discon}}$ the light and strange quark disconnected diagrams, $\mathcal{H}^{\mathrm{subleading\text{-}discon}}$ the light and strange quark subleading disconnected diagrams [vanish in the flavor SU(3) limit], and $\mathcal{H}^{\mathrm{charm}}$ all diagrams involving charm quark loops.

Naturally, after the Wick contraction, $\mathcal{H}$ defined in Eq. (15) can be expressed in terms of quark propagators and includes all permutations of x, y, and z. However, note that all other terms in the master formula Eq. (8) are symmetric with respect to permutations of x, y, and z (along with its Lorentz indices). Therefore, we are allowed to calculate only a subset of the diagrams generated by the Wick contractions in Eq. (15) and multiply them with appropriate factors.

$$\begin{aligned} &6e^4\mathcal{H}^{\mathrm{con}}_{\nu,\rho,\sigma,\kappa}(x_{\mathrm{op}},x,y,z) \\ &\Rightarrow 6e^4\mathcal{H}^{\mathrm{con\text{-}no\text{-}perm}}_{\nu,\rho,\sigma,\kappa}(x_{\mathrm{op}},x,y,z) \\ &= -6\Big\langle \mathrm{Re}\sum_{q=u,d,s} e_q^4 \mathrm{Tr}(\gamma_\nu S_q(x_{\mathrm{op}},x)\gamma_\rho S_q(x,z) \\ &\quad\times\gamma_\kappa S_q(z,y)\gamma_\sigma S_q(y,x_{\mathrm{op}}))\Big\rangle_{\mathrm{QCD}}, \end{aligned} \tag{18}$$

$$\begin{aligned} &6e^4\mathcal{H}^{\mathrm{discon}}_{\nu,\rho,\sigma,\kappa}(x_{\mathrm{op}},x,y,z) \\ &\Rightarrow 6e^4\mathcal{H}^{\mathrm{discon\text{-}no\text{-}perm}}_{\nu,\rho,\sigma,\kappa}(x_{\mathrm{op}},x,y,z) \\ &= 3\Big\langle \sum_{q'=u,d,s} e_{q'}^2 \mathrm{Tr}(\gamma_\nu S_{q'}(x_{\mathrm{op}},x)\gamma_\rho S_{q'}(x,x_{\mathrm{op}})) \\ &\quad\times\sum_{q=u,d,s} e_q^2 \mathrm{Tr}(\gamma_\kappa S_q(z,y)\gamma_\sigma S_q(y,z) \\ &\quad-\langle\gamma_\kappa S_q(z,y)\gamma_\sigma S_q(y,z)\rangle_{\mathrm{QCD}})\Big\rangle_{\mathrm{QCD}}, \end{aligned} \tag{19}$$

where S_q denotes the quark propagator. As shown in Fig. 4, we calculate the hadronic four-point function with two point-source propagators. The above trick can make the evaluation more efficient [42,47]. We note that $\mathcal{H}^{\mathrm{discon\text{-}no\text{-}perm}}$, the disconnected diagram of the hadronic four-point function without permutation, still satisfies the current conservation condition in the continuum limit (this is not true for $\mathcal{H}^{\mathrm{con\text{-}no\text{-}perm}}$) which leads to the following relation in the infinite volume limit:

$$\sum_{x_{\mathrm{op}}}\mathcal{H}^{\mathrm{discon\text{-}no\text{-}perm}}_{k,\rho,\sigma,\lambda}(x_{\mathrm{op}},x,y,z)=0. \tag{20}$$

We are therefore allowed to alter the choice of x_{ref} for the disconnected diagram

$$x_{\mathrm{ref\text{-}discon}}=x. \tag{21}$$

This choice allows the summation over x_{op} to be performed independently of coordinates y and z. This choice also has the benefit of suppressing the contribution from the region

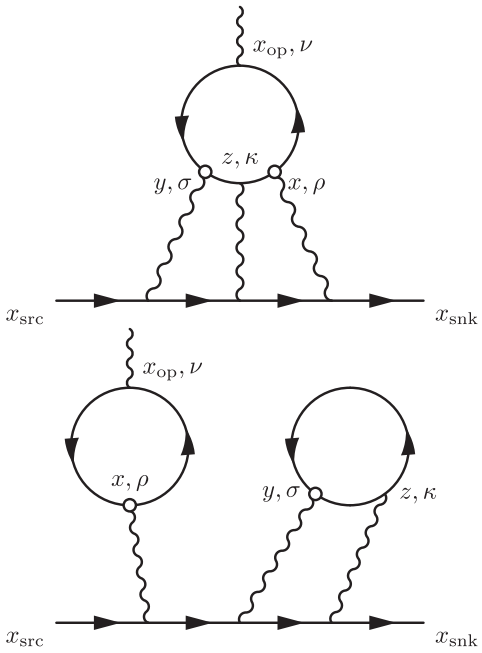

FIG. 4. Two point-source propagators are used to calculate the hadronic four-point function. The locations of the point-sources are indicated in the diagrams as small circles.

where $|x - x_{\mathrm{op}}|$ is small and the quark loop is large before subtracting the vacuum expectation value. Also, we note that the new choice $x_{\text{ref-discon}}$ is the same as the initial choice in the long distance region where the contribution is dominated by π^0-exchange and $|y - z| \ll \min(|x - y|, |x - z|)$. This property guarantees that the connected and disconnected diagrams have exactly the same QED weighting function in the long distance region, which leads to Eq. (28) before taking the continuum limit. This is the main reason for the choice of x_{ref} for the connected diagrams.

III. LATTICE DETAILS

The calculation presented here is performed on ensembles of gauge fields generated by the RBC and UKQCD collaborations [52]. The main calculation is carried out using the 48I ensemble, a physical-mass ensemble generated with $2 + 1$ flavors of Möbius domain wall fermions (MDWF). We also use a few other ensembles to calculate various corrections and estimate systematic effects. The relevant information about the 48I ensemble and other ensembles is listed in Table I. We always use the MDWF action. For most of the ensembles, the quarks have their physical masses.

For our main calculation on the 48I ensemble, we use 113 configurations. On each configuration, we randomly sample 2048 uniformly distributed distinct points and calculate light quark point-source propagators for each of the selected points.

Among the above 2048 points we randomly select 1024 points and also calculate strange quark propagators. These $2048 + 1024$ point-source propagators are computed using the (deflated-) conjugate gradient algorithm with a sloppy stopping condition. To further speed up the sloppy propagator calculation, we use the zMöbius domain wall fermion formulation [54] with reduced fifth dimension size $L_s = 14$ to approximate the unitary MDWF action used in the gauge ensemble generation ($L_s = 24$). For deflation of the Dirac operator we reuse the eigenvectors generated for the calculation of the hadronic vacuum polarization contribution to the muon $g-2$ [55,56] using the locally coherent Lanczos approach [57]. Then, we use a two-level all-mode-averaging (AMA) method [58] to correct the bias caused by the inexact propagators. The AMA method requires a portion of the sloppy propagators be computed again with higher precision. In the first step a more precise version of the light and strange quark propagators are calculated on a randomly selected set of 64 points among the 1024 points. In the second step among the 64 points, we randomly select 16 points and calculate these propagators to full precision. These propagators are used to calculate both the connected and the disconnected diagrams in the bias correction. By using two steps, we are able to reduce the statistical error coming from the bias correction to a level well below the statistical error for the sloppy part.

For the connected diagrams, we sample two-point pairs among all the possible $2048 \times (2048 - 1)/2 + 2048 = 2098176$ combinations (including the case where $x = y$). For each of the two-point pairs, we can perform the contraction as described in Eq. (18) in the previous section. As the number of all possible pairs is enormous, the cost to perform all the contractions is not affordable. Therefore, we only calculate the contraction for a subset of the available two-point pairs. We sample the subset with the empirical probability $p(r)$, which is a function of the distance between the two points, $r = |x - y|$,

$$p(r) = \begin{cases} \frac{N_{\mathrm{psrc}}-1}{2(L^3T-1)} & \text{if } r = 0 \\ 1 & \text{if } 8 \geq r > 0 \\ \frac{1}{(r/8)^3} & \text{if } L \geq r > 8 \\ 0 & \text{if } r > L \end{cases}, \tag{22}$$

where $L = 48$, $T = 96$, and the numbers are in lattice units. On average, about 57,000 light quark point-source propagator pairs per configuration are sampled to calculate the connected diagrams. The reason we sample long-distance point-pairs less often is because the connected hadronic four point function and its statistical fluctuation decrease with distance for long distances. For each pair, due to the sampling procedure, the probability of that pair taking a particular relative coordinate is a function of r. The total connected diagram contribution is equal to the expectation value of the contraction for the point pairs multiplied by the inverse probabilities. We refer to the inverse probability as the weight $w(r)$

TABLE I. $2+1$ flavors of MDWF gauge field ensembles generated by the RBC-UKQCD collaborations [52]. The labels indicate the lattice size in lattice units and the QCD gauge action, where "I" stands for Iwasaki, and "D" stands for Iwasaki + DSDR. DSDR stands for dislocation-suppressing-determinant-ratio, which is an additional term in the action to soften explicit chiral symmetry breaking effects, needed in particular for very coarse lattices [53]. The pion mass m_π, lattice spacing a[a], spatial extent L, extra fifth dimension size L_s, and the number of QCD configurations used are listed.

	48I	64I	24D	32D	24DH
m_π (MeV)	139	135	142	142	341
a^{-1} (GeV)	1.730	2.359	1.015	1.015	1.015
a (fm)	0.114	0.084	0.194	0.194	0.194
L (fm)	5.47	5.38	4.67	6.22	4.67
L_s	24	12	24	24	24
No. meas	113	64	31	70	37

[a]After the analysis for this work was completed, we updated the lattice spacing for the 24D and 32D ensembles. The new lattice spacing is $a^{-1} = 1.023$ GeV and makes no material difference to the results presented here.

$$w(r) = \begin{cases} w_0 & \text{if } r = 0 \\ w_0/p(r) & \text{if } r > 0 \end{cases}, \tag{23}$$

$$w_0 = \sum_x p(|x|). \tag{24}$$

To further reduce the contraction cost and the storage cost of saving these propagators, we use field sparsening techniques [59,60]. We randomly sample $1/16$ points among all the points of the lattice and only perform contractions on these randomly selected points. Since we only need propagator values on these points, we only save these values to disk. To accommodate the sparsening, we multiply a factor of 16^2 for the summation over z and x_{op} in Eq. (8), except when $z = x_{\text{op}}$, where we multiply by 16. In this way the sampling procedure does not introduce any systematic effects on our central value.

For the disconnected diagrams, the two point-source locations are also indicated in Fig. 4. Different from the connected diagrams, the statistical fluctuations of the disconnected hadronic functions are not suppressed when $r = |x - y|$ increases. Therefore, we use all possible combinations of point pairs of x and y as long as $|x - y| \le L$ to estimate the summation over x and y in Eq. (8). Thanks to the choice of $x_{\text{ref}} = x_{\text{ref-discon}} = x$ in Eq. (21), the summation over x_{op} can be performed for each point-source propagator with source location at x, the result can be used for all possible values of y locations. However, the summation of z depends on the location of x and y due to the QED weighting function. Therefore, we need to perform the summation over z for each pair of points.

To make the contractions of all point pairs affordable, we aggressively sparsen when summing over z. Fortunately, the vertex z and vertex y are connected by two quark propagators, and the four point function is exponentially suppressed when the distance between z and y increases.

Naturally, we can sample the z locations based on the distance between z and y, similar to the sampling of x and y combinations in the calculation of the connected diagrams. However, for this disconnected diagram, we discovered a much more efficient adaptive sampling scheme as follows. For each point-source location y, we calculate the following square norm $n(z, y)$ of the quark loop for all z:

$$n(z,y) = \sum_{\kappa,\sigma} |\text{Tr}(\gamma_\kappa S_q(z,y)\gamma_\sigma S_q(y,z) - \langle \gamma_\kappa S_q(z,y)\gamma_\sigma S_q(y,z)\rangle_{\text{QCD}})|^2$$

Unlike the full contraction, the above norm is independent of the location of x, and the location of z is sampled with the following (empirical) probability

$$p_y(z) = \begin{cases} 1 & \text{if } n(z,y) \ge t_0^2 \quad \text{and} \quad |z-y| \le L \\ \sqrt{n(z,y)}/t_0 & \text{if } n(z,y) < t_0^2 \quad \text{and} \quad |z-y| \le L \\ 0 & \text{if } |z-y| > L \end{cases}, \tag{25}$$

where t_0 is the threshold parameter to control the overall sample frequency. With this probability distribution, we sample more often points where the (norm of) the quark loop is large which is much more efficient than basing the probability on the distance $|z - y|$. We choose $t_0 = 5 \times 10^{-5}$ in this work for the 48I ensemble.

For the light quark loop, there are 9,156,431 points within the $|z - y| \le L$ range. Among these, we sample about 17,000 points for z on average. For each of the sampled z, we then loop over all possible x locations with $|x - y| \le L$ and perform the full contraction. Due to the sampling procedure, we multiply the result of the contraction by the inverse of the sample probability $1/p_y(z)$ to obtain an unbiased final result. While the sampled z points amount to less than 0.2% of the possible z points in the allowed range, we expect the final statistical precision to be almost unaffected by the adaptive sampling procedure. That is, we expect the final statistical error would be almost the same even if we had calculated the contraction using all the z locations. This expectation is based on a quick test run with much lower threshold $t_0 = 10^{-3}$, which corresponds to about a factor of 20 smaller number of sampled points; we find the final statistical error is roughly the same.

In contrast to the connected diagram, we do not sparsen the propagators. To save disk space, we temporarily save the following intermediate contraction for each point-source propagator:

$$\text{Tr}(\gamma_\kappa S_q(z,y)\gamma_\sigma S_q(y,z)). \tag{26}$$

For each propagator on each lattice site, the above contraction corresponds to 4×4 complex numbers while the full propagator takes 12×12 complex numbers.

IV. RESULTS

In this section we display several figures of the summand (integrand) or its partial sum as a function of R_{max}

$$R_{\mathrm{max}} = \max(|x-y|, |y-z|, |x-z|), \tag{27}$$

where x, y, and z represent the positions of the three internal quark-photon vertices. Partial sums are obtained by summing the corresponding summand from 0 up to the specified value of R_{max} (inclusive). The rightmost value in a partial-sum plot corresponds to the total contribution.

Since the summand decreases exponentially at large R_{max}, we expect the partial sum to approach a plateau for large enough R_{max}. We usually use the result of the partial sum at 4 fm, which includes all contributions from the region $R_{\mathrm{max}} < 4$ fm. In the lattice calculation, we calculate the partial sum with respect to R_{max} and save the partial sum for all integer values (in lattice units) of the upper limit of R_{max}. To compare with results calculated using ensembles with different lattice spacings, we can linearly interpolate the partial sum for any upper limit of R_{max}. In this work, we choose to interpolate at integer multiples $\times 0.1$ fm. The summand is obtained at half-integer multiples $\times 0.1$ fm by taking the difference of the linearly interpolated partial sum. Therefore, the data points of the plots shown in this work always have spacing 0.1 fm, and the data points of the integrand plots always have its x-axis value equal to half-integer times 0.1 fm. In this work, we present our results for the anomalous magnetic moment in the unit of 10^{-10}.

A. Light quark contribution

The contributions from the connected diagrams, the disconnected diagrams, and the sum of the two contributions are shown in Fig. 5. As can be seen from the figure, the statistical error grows as R_{max} increases. However, for both the connected and the disconnected diagrams, there are non-negligible contributions that come from regions where R_{max} is as large as 3 or 4 fm. The statistical error is quite significant. Making the situation worse, the contributions from the long-distance region of the connected and the disconnected diagrams are opposite in sign, while the statistical error of the connected and the disconnected diagrams are largely independent. As a result, the relative uncertainty on the sum is much larger than that for the individual contributions. Results are given in Table II as "48I light con $R_{\mathrm{max}} < 4$ fm," "48I light discon $R_{\mathrm{max}} < 4$ fm," and "48I light $R_{\mathrm{max}} < 4$ fm."

To improve the situation, note that the large contribution and the cancellation between the connected and disconnected diagrams at long distance are due to π^0 exchange and are well-understood theoretically [48,61,62]. It has been shown that, at large R_{max}, the ratio of the disconnected

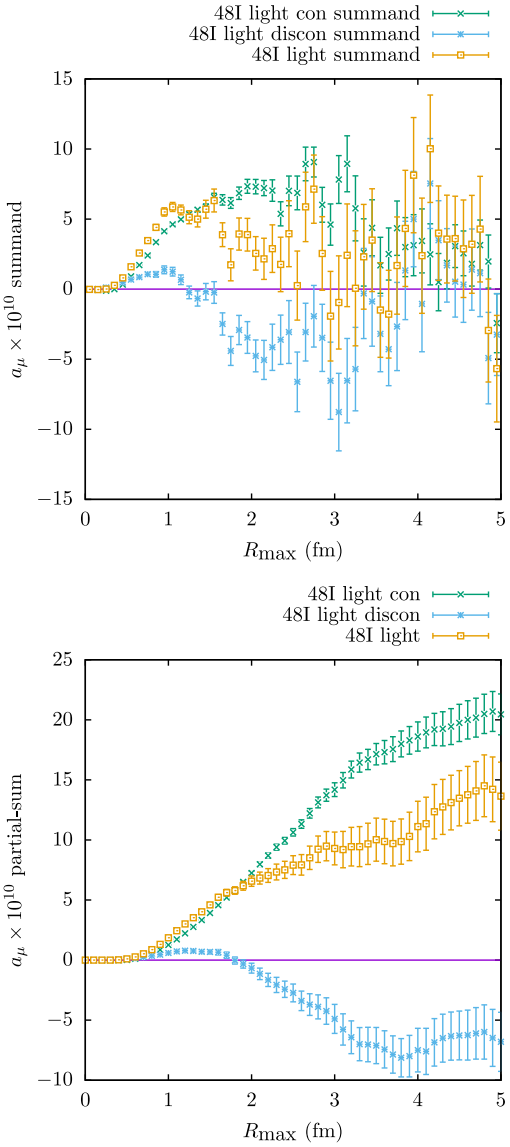

FIG. 5. Light quark contributions computed on the 48I ensemble from the connected diagrams, the disconnected diagrams, and the total. The upper plot shows the corresponding summands and the lower plot shows the partial sum.

and the connected hadronic four-point function is $-25/34$. In our present computational setup, we use the same infinite volume QCD weighting function for both the connected and disconnected diagrams, and use the same variable R_{max} to study the partial sum of the connected and disconnected diagrams. [63] Therefore the same ratio applies to the contribution to a_μ. Formally, we have

$$\lim_{R\to\infty} \frac{a_\mu^{\mathrm{discon}}(R_{\mathrm{max}} > R)}{a_\mu^{\mathrm{con}}(R_{\mathrm{max}} > R)} = -\frac{1}{2} \cdot \frac{(e_u^2 + e_d^2)^2}{e_u^4 + e_d^4} = -\frac{25}{34}. \tag{28}$$

Here, R_{max} is defined in Eq. (27), being a function of the three vertex locations x, y, z as shown in Fig. 4. The long-distance contributions for the connected and disconnected diagrams

TABLE II. Light quark contributions computed on the 48I ensemble. Values are different contributions to $a_\mu \times 10^{10}$ where $a_\mu = (g_\mu - 2)/2$. The numbers in the square bracket are the statistical and systematic uncertainty combined in quadrature. The tag "hybrid-" indicates the same quantity obtained using the hybrid approach.

Contribution name	$a_\mu \times 10^{10}$
48I light con $R_{\max} < 2$ fm	$7.24\ (0.15)_{\text{stat}}$
48I light con $R_{\max} < 2.5$ fm	$10.64\ (0.31)_{\text{stat}}$
48I light con $R_{\max} < 4$ fm	$18.61\ (1.22)_{\text{stat}}$
48I light con $R_{\max} > 4$ fm	$7.56\ (0.42)_{\text{stat}}(1.06)_{\text{syst}}[1.14]$
48I light con FV-corr	$-1.79\ (0.42)_{\text{syst}}$
48I light con m_π-corr	$1.32\ (0.27)_{\text{stat}}(0.66)_{\text{syst}}[0.72]$
48I light con a^2-corr	$0.00\ (1.49)_{\text{syst}}$
light con	$25.70\ (1.33)_{\text{stat}}(1.99)_{\text{syst}}[2.39]$
48I light no-pion $R_{\max} < 2.5$ fm	$5.09\ (0.76)_{\text{stat}}$
48I light no-pion $R_{\max} < 2$ fm	$4.65\ (0.42)_{\text{stat}}$
48I light no-pion $R_{\max} > 2.5$ fm	$0.31\ (0.22)_{\text{stat}}(0.31)_{\text{syst}}[0.38]$
48I light no-pion $R_{\max} > 2$ fm	$0.88\ (0.46)_{\text{stat}}(0.88)_{\text{syst}}[0.99]$
48I light discon $R_{\max} < 2$ fm	$-0.67\ (0.41)_{\text{stat}}$
48I light discon $R_{\max} < 2.5$ fm	$-2.73\ (0.74)_{\text{stat}}$
48I light discon $R_{\max} < 4$ fm	$-7.49\ (1.82)_{\text{stat}}$
48I light discon $R_{\max} < 4$ fm hybrid-2.5 fm	$-8.28\ (1.31)_{\text{stat}}(0.31)_{\text{syst}}[1.35]$
48I light discon $R_{\max} < 4$ fm hybrid-2 fm	$-8.15\ (1.24)_{\text{stat}}(0.88)_{\text{syst}}[1.51]$
48I light discon $R_{\max} > 4$ fm	$-5.56\ (0.31)_{\text{stat}}(0.78)_{\text{syst}}[0.84]$
48I light discon FV-corr	$1.31\ (0.31)_{\text{syst}}$
48I light discon m_π-corr	$-0.98\ (0.20)_{\text{stat}}(0.49)_{\text{syst}}[0.53]$
48I light discon a^2-corr	$0.00\ (0.66)_{\text{syst}}$
light discon	$-12.71\ (1.87)_{\text{stat}}(1.17)_{\text{syst}}[2.20]$
light discon hybrid-2.5 fm	$-13.50\ (1.36)_{\text{stat}}(1.21)_{\text{syst}}[1.82]$
light discon hybrid-2 fm	$-13.37\ (1.29)_{\text{stat}}(1.46)_{\text{syst}}[1.95]$
48I light $R_{\max} < 2$ fm	$6.57\ (0.43)_{\text{stat}}$
48I light $R_{\max} < 2.5$ fm	$7.90\ (0.78)_{\text{stat}}$
48I light $R_{\max} < 4$ fm	$11.11\ (2.11)_{\text{stat}}$
48I light $R_{\max} < 4$ fm hybrid-2.5 fm	$10.32\ (0.99)_{\text{stat}}(0.31)_{\text{syst}}[1.04]$
48I light $R_{\max} < 4$ fm hybrid-2 fm	$10.46\ (0.89)_{\text{stat}}(0.88)_{\text{syst}}[1.25]$
48I light $R_{\max} > 4$ fm	$2.00\ (0.11)_{\text{stat}}(0.28)_{\text{syst}}[0.30]$
48I light FV-corr	$-0.47\ (0.11)_{\text{syst}}$
48I light m_π-corr	$0.35\ (0.07)_{\text{stat}}(0.17)_{\text{syst}}[0.19]$
48I light a^2-corr	$0.00\ (0.83)_{\text{syst}}$
light total	$12.99\ (2.11)_{\text{stat}}(0.90)_{\text{syst}}[2.29]$
light total hybrid-2.5 fm	$12.20\ (1.01)_{\text{stat}}(0.95)_{\text{syst}}[1.38]$
light total hybrid-2 fm	$12.33\ (0.90)_{\text{stat}}(1.25)_{\text{syst}}[1.55]$

are denoted as $a_\mu^{\text{con}}(R_{\max} > R)$ and $a_\mu^{\text{discon}}(R_{\max} > R)$. They can be calculated with the same summation as in Eq. (8) but with the additional constraint that $R_{\max} > R$, where R is the long-distance cutoff. Note we take the $R \to \infty$ limit in the above equation. This ratio is exact in this limit and is not affected by lattice artifacts or finite volume effects. Therefore, we can construct the following combination:

$$a_\mu^{\text{no-pion}} = a_\mu^{\text{discon}} + \frac{25}{34} a_\mu^{\text{con}}, \tag{29}$$

where the π^0 exchange contribution to $a_\mu^{\text{no-pion}}$ vanishes in the long distance. We plot the summand and partial sum of $a_\mu^{\text{no-pion}}$ in Fig. 6. Indeed, the partial sum of $a_\mu^{\text{no-pion}}$ reaches the plateau much earlier than the connected or disconnected diagrams. This trick of combining the connected and disconnected with appropriate factors to obtain a faster plateau was employed in Ref. [64]. For $a_\mu^{\text{no-pion}}$, we will use 2.0 and 2.5 fm as the upper limit of $R_{\max}$. The results are shown in Table II as "48I light no-pion $R_{\max} < 2.5$ fm" or "48I light no-pion $R_{\max} < 2$ fm."

In the upper panel of Fig. 6, we fit the summand to the following empirical form:

$$f(R_{\max}) = A/\text{fm}^4 \frac{R_{\max}^6}{R_{\max}^3 + (C\,\text{fm})^3} e^{-BR_{\max}/(\text{fm}\cdot\text{GeV})} \tag{30}$$

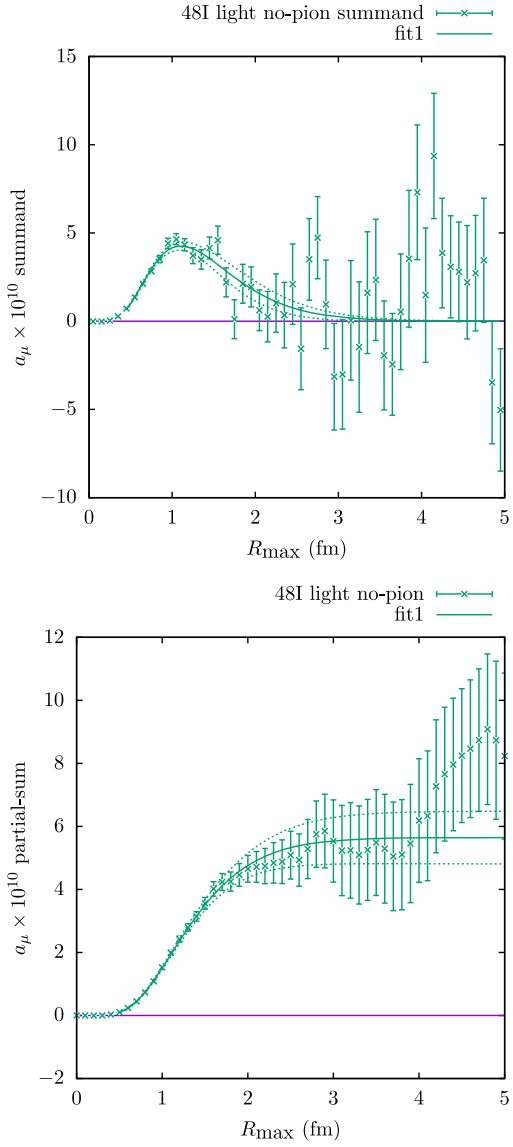

FIG. 6. Light quark contributions from a special combination of the connected and disconnected diagrams to cancel the long-distance π^0 exchange contribution [see Eq. (29)]. The upper plot shows the summand and the lower plot shows the partial sum. The combined summand vanishes much faster than the light quark diagrams by themselves. Solid curves represent a fit of the data to Eq. (30). The fit starts at 0.5 fm. The dashed lines denote the statistical uncertainty of the fit.

The fit range is from 0.5 to 4 fm. We use the result of the fit to estimate the long-distance contribution to $a_\mu^{\text{no-pion}}$. Since this is a completely empirical fit, we will assign a 100% systematic uncertainty to it. The "no-pion" results are also collected in Table II.

With the definition of $a_\mu^{\text{no-pion}}$, we obtain

$$a_\mu^{\text{discon}} = a_\mu^{\text{no-pion}} - \frac{25}{34} a_\mu^{\text{con}}, \tag{31}$$

$$a_\mu^{\text{total}} = a_\mu^{\text{no-pion}} + \frac{9}{34} a_\mu^{\text{con}}. \tag{32}$$

The advantage comes in using the early plateau value of $a_\mu^{\text{no-pion}}$ and combining it with a_μ^{con}, which plateaus at much larger $R_{\max}$. This is a "hybrid" approach to calculate a_μ^{discon} and a_μ^{total}, which has a much smaller statistical error than the direct combination. For a_μ^{con}, we will use 4 fm as the upper limit of $R_{\max}$. The results are shown in Table II as entries that start with "48I light discon $R_{\max} < 4$ fm hybrid-" and "48I light $R_{\max} < 4$ fm hybrid-."

The fitting function form in Eq. (30) is inspired by the function in Eq. (20) of Ref. [48]. The functional form used here differs due to the meanings of $R_{\max}$ and the variable "$|y|$" in Ref. [48]. Also, note that the subtraction scheme of the QED weighting function is also different [46–48,65]. We tried using this fit function to fit other contributions. The results are shown in Appendix C.

The statistical errors are estimated by assuming the results from each 48I configuration that we performed the measurements are statistically independent. We also tried to bin the data with different lengths in MD time units. The results are shown in Table III. We can see that the statistical error does not significantly depend on the binning sizes. More interestingly, the statistical error calculated by assuming all the individual samples in each configuration are independent is only a little bit smaller than the statistical error calculated from the fluctuation of different configurations. This implies that the current statistical errors still mainly come from the sampling of the points from each configuration, instead of from the gauge field fluctuations sampled by different gauge configurations. Also, this shows that the strategy using different combinations of the point source propagators as point pairs to calculate the connected diagrams is very effective.

The remaining finite volume, pion mass, and nonzero lattice spacing corrections will be studied in Secs. IV D–IV F.

B. Strange quark contribution

The contributions from the strange quark connected diagrams, the disconnected diagrams, and the sum of the two contributions are plotted in Fig. 7. Note the strange quark disconnected diagrams include diagrams where one or both loops are strange quark loops, while the light quark disconnected diagrams discussed in the previous section contain only light quarks. As seen in the figure, the contribution from the strange quark-connected diagrams is very precise and very small. It can also be clearly seen that the strange quark contribution vanishes much faster at long-distance compared to the light quark contribution.

The disconnected diagrams, on the other hand, are much noisier. However, we still expect the signal to vanish faster than the light quark contribution due to the absence of the

TABLE III. Two light quark contributions computed on the 48I ensemble. The table lists the statistical errors calculated with different binning sizes in MD time units in the HMC evolutions. The separation between the configurations we performed the measurements is 10 MD time units. The last column named "Bin(sample)" list the statistical error calculated by assuming all the individual samples in each configuration are independent. The samples for the connected diagrams are the point pairs, where we have about 57,000 pairs for each configuration. The samples for the disconnected diagrams are the points for y in Fig. 4 (summation over x is already performed), where we have about 2048 points for each configuration.

Contribution name	$a_\mu \times 10^{10}$	Bin(20)	Bin(30)	Bin(40)	Bin(sample)
48I light con $R_{\text{max}} < 4$ fm	18.61 (1.22)	1.30	1.15	1.24	1.15
48I light discon $R_{\text{max}} < 2.5$ fm	−2.73 (0.74)	0.79	0.84	0.75	0.65

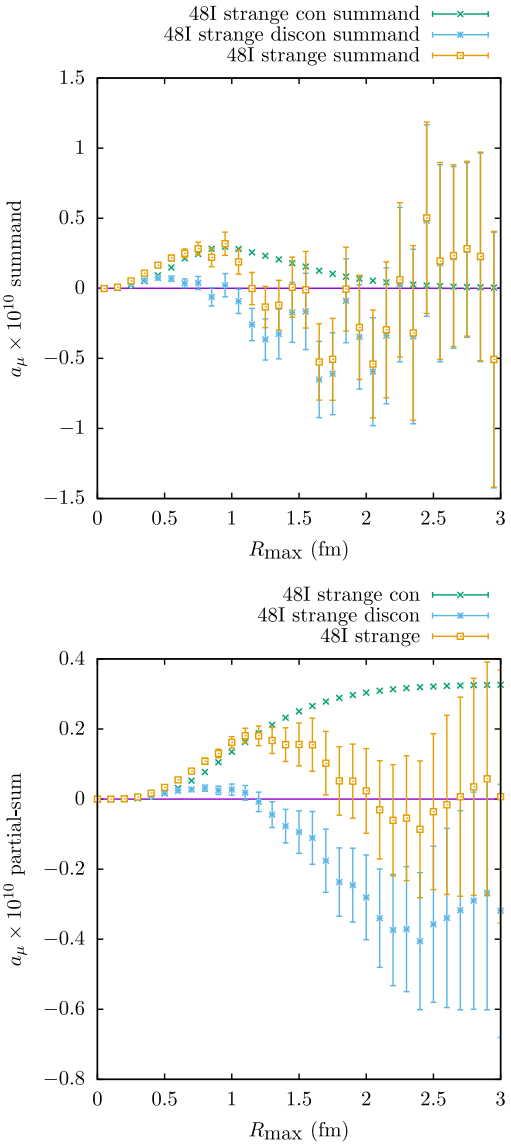

FIG. 7. Strange quark contributions computed on the 48I ensemble from the connected diagrams, the disconnected diagrams, and the total. The upper plot shows the corresponding summands and the lower plot shows the partial sum.

π^0 exchange contribution. Therefore, we can treat the strange quark disconnected diagrams as similar to $a_\mu^{\text{no-pion}}$. We listed the results with 4.0, 2.5, and 2 fm as the upper limit of R_{max}. These results are shown in Table IV as entries that start with "48I strange discon $R_{\text{max}} <$." We estimate the systematic error caused by truncating the strange quark disconnected diagram integration using the size of the long-distance contribution from the strange quark connected diagrams, which is also shown in Table IV as entries that start with "48I strange con $R_{\text{max}} >$." The size of the long-distance connected contribution is used as the estimation for the systematic uncertainty for the corresponding disconnected contributions.

The remaining finite volume, pion mass, and nonzero lattice spacing corrections will be studied in Secs. IV D–IV F.

C. Long-distance π^0-exchange contribution

The dominant source of the HLbL contribution is expected to be the so-called "π^0-pole" contribution [5]. Due to the small mass of the π^0, this contribution can be non-negligible for large R_{max} in a Euclidean space-time lattice calculation, even where long-distance contributions and finite volume effects are exponentially suppressed since it is only suppressed as $e^{-m_\pi R_{\text{max}}}$.

We separately calculate the long-distance π^0-exchange contribution as illustrated in Fig. 8. We use the lattice calculation of the π^0 transition form factor

$$\mathcal{F}_{\mu,\nu}(x,p) = \langle 0|TJ_\mu(x)J_\nu(0)|\pi^0(\vec{p})\rangle \tag{33}$$

$$= \epsilon_{\mu,\nu,\rho,\sigma} x_\rho p_\sigma \mathcal{F}(x^2, p\cdot x), \tag{34}$$

where p is the Euclidean four-momentum of the π^0 state. We use $p = (im_\pi, \vec{0}) = im_\pi \hat{t}$ in the numerical lattice calculation. So we can obtain the numerical values of

$$\mathcal{F}_{\mu,\nu}(x, im_\pi \hat{t}) \tag{35}$$

for all possible Euclidean space-time locations x directly from lattice QCD calculations, without assuming any

TABLE IV. Strange quark contributions computed on the 48I ensemble. Values are different contributions to $a_\mu \times 10^{10}$ where $a_\mu = (g_\mu - 2)/2$. The numbers in the square bracket are the statistical and systematic uncertainty combined in quadrature. The "strange discon" contribution includes disconnected diagrams where one or two loops are strange quark loops. The tag "hybrid-" indicates the same quantity obtained using the hybrid approach.

Contribution name	$a_\mu \times 10^{10}$
48I strange con $R_{\text{max}} < 4$ fm	$0.327\ (0.002)_{\text{stat}}$
48I strange con a^2-corr	$0.026\ (0.008)_{\text{stat}}$
Strange con	$0.353\ (0.007)_{\text{stat}}$
48I strange con $R_{\text{max}} > 2.5$ fm	$0.006\ (0.000)_{\text{stat}}$
48I strange con $R_{\text{max}} > 2$ fm	$0.024\ (0.000)_{\text{stat}}$
48I strange discon $R_{\text{max}} < 4$ fm	$-0.380\ (0.607)_{\text{stat}}$
48I strange discon $R_{\text{max}} < 2.5$ fm	$-0.357\ (0.223)_{\text{stat}}$
48I strange discon $R_{\text{max}} < 2$ fm	$-0.280\ (0.121)_{\text{stat}}$
48I strange discon a^2-corr	$0.000\ (0.029)_{\text{syst}}$
Strange discon	$-0.380\ (0.607)_{\text{stat}}(0.029)_{\text{syst}}[0.608]$
Strange discon hybrid-2.5 fm	$-0.357\ (0.223)_{\text{stat}}(0.029)_{\text{syst}}[0.225]$
Strange discon hybrid-2 fm	$-0.280\ (0.121)_{\text{stat}}(0.037)_{\text{syst}}[0.126]$
48I strange $R_{\text{max}} < 4$ fm	$-0.053\ (0.607)_{\text{stat}}$
48I strange $R_{\text{max}} < 4$ fm hybrid-2.5 fm	$-0.030\ (0.222)_{\text{stat}}(0.006)_{\text{syst}}[0.223]$
48I strange $R_{\text{max}} < 4$ fm hybrid-2 fm	$0.047\ (0.121)_{\text{stat}}(0.024)_{\text{syst}}[0.123]$
48I strange a^2-corr	$0.026\ (0.008)_{\text{stat}}(0.029)_{\text{syst}}[0.030]$
Strange total	$-0.027\ (0.607)_{\text{stat}}(0.029)_{\text{syst}}[0.608]$
Strange total hybrid-2.5 fm	$-0.004\ (0.223)_{\text{stat}}(0.029)_{\text{syst}}[0.225]$
Strange total hybrid-2 fm	$0.073\ (0.121)_{\text{stat}}(0.037)_{\text{syst}}[0.127]$

particular function form for the transition form factor. This form factor can then be used to construct approximations for infinite volume hadronic correlation functions with large separation. A detailed derivation is given in Appendix B. Here, we briefly describe the idea. First, we introduce a properly normalized π^0 interpolating field, e.g.,

$$\pi^0(x) = Z_\pi^{1/2} \frac{i}{\sqrt{2}} (\bar{u}(x)\gamma_5 u(x) - \bar{d}(x)\gamma_5 d(x)). \quad (36)$$

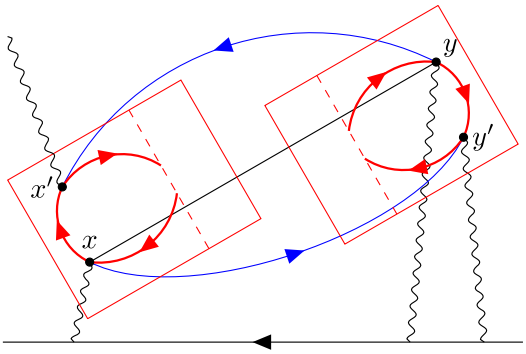

FIG. 8. The long-distance HLbL contribution to the muon $g-2$ associated with π^0 exchange. The amplitudes inside the boxes are calculated in lattice QCD while the pion propagator linking them (solid lines) is given by the analytic, infinite-volume, continuum expression.

The normalization constant Z_π is determined by the following requirement:

$$\langle 0|\pi^0(x)|\pi^0(\vec{p})\rangle = e^{ip\cdot x}. \quad (37)$$

We can then rewrite Eq. (33) in a slightly different form

$$\langle 0|TJ_\mu(x)J_\nu(y)|\pi^0(\vec{p})\rangle = \mathcal{F}_{\mu,\nu}(x-y,p)\langle 0|\pi^0(y)|\pi^0(\vec{p})\rangle. \quad (38)$$

The above relation suggest that the time-ordered product $TJ_\mu(x)J_\nu(y)$, when used in between the vacuum state and a single π^0 state, can be viewed as a properly weighted π^0 interpolating field: $\mathcal{F}_{\mu,\nu}(x-y,p)\pi^0(y)$. This property can be used to calculate the following three-point function:

$$\langle TJ_\mu(x)J_\nu(y)\pi^0(z)\rangle \quad (39)$$

For very large $m_\pi|y-z|$ and $y-z$ along the positive time direction, i.e. $y-z = (|y-z|,\vec{0})$, the intermediate states between $TJ_\mu(x)J_\nu(y)$ and $\pi^0(z)$ will be mostly π^0 states with $\vec{p} \approx \vec{0}$. We can employ Eq. (38) with $p \approx (im_\pi, \vec{0})$ and obtain:

$$\langle TJ_\mu(x)J_\nu(y)\pi^0(z)\rangle \approx \mathcal{F}_{\mu,\nu}\left(x-y, im_\pi \frac{y-z}{|y-z|}\right) \times \langle T\pi^0(y)\pi^0(z)\rangle. \quad (40)$$

Note that we have expressed the above relation in an $O(4)$ rotationally covariant form, so the equation is also valid for $y-z$ in directions other than the time direction. Then, we can introduce the infinite-volume free scalar propagator $D_{\pi^0}(z)$, with physical pion mass. For sufficiently large $|x-y|$, we have

$$\langle T\pi^0(x)\pi^0(y)\rangle = D_{\pi^0}(x-y). \tag{41}$$

Now, the relation between Eqs. (33) and (40) is established. We can approximate the infinite volume hadronic four-point function illustrated in Fig. 8 in the large $|x-y|$ region in a similar approach

$$\begin{aligned}\langle TJ_{\mu'}(x')J_{\mu}(x)J_{\nu'}(y')J_{\nu}(y)\rangle \approx D_{\pi^0}(x-y)\\ \times \mathcal{F}_{\mu',\mu}\left(x'-x, im_\pi\frac{x-y}{|x-y|}\right)\\ \times \mathcal{F}_{\nu',\nu}\left(y'-y, im_\pi\frac{y-x}{|y-x|}\right).\end{aligned} \tag{42}$$

In the above approximation, $|x-x'|$ and $|y-y'|$ will not be too large in order to create localized pion states, so the form factor $\mathcal{F}$ can be computed using a reasonably sized lattice. As described in Eqs. (33) and (35), we only directly calculate the transition form factor $\mathcal{F}$ for a zero-momentum pion state. To obtain the form factor needed in Eq. (42) above, we need to perform $O(4)$ rotations

$$\mathcal{F}_{\mu,\nu}(\tilde{x}, im_\pi\hat{n}) = \Lambda_{\mu,\mu'}\Lambda_{\nu,\nu'}\mathcal{F}_{\mu',\nu'}(\tilde{x}', im_\pi\hat{t}), \tag{43}$$

where $\tilde{x}$ can be either $x'-x$ or $y'-y$ in Eq. (42) and $\hat{n}$ can be $\pm(x-y)/|x-y|$. The $O(4)$ rotation matrix $\Lambda=\Lambda(\hat{n})$ and Euclidean space-time coordinate $\tilde{x}'$ satisfy

$$\delta_{\mu,\nu} = \Lambda_{\mu,\mu'}\Lambda_{\nu,\nu'}\delta_{\mu',\nu'}, \tag{44}$$

$$\hat{n}_\mu = \Lambda_{\mu,\mu'}\hat{t}_{\mu'}, \tag{45}$$

$$\tilde{x}_\mu = \Lambda_{\mu,\mu'}\tilde{x}'_{\mu'}. \tag{46}$$

We would like to emphasize again that we do not assume any particular form of the π^0 transition form factor and perform fits. The inputs to Eq. (42) can be directly obtained from the $O(4)$ rotation in Eq. (43) and the lattice QCD calculation of the position-space matrix elements $\mathcal{F}_{\mu,\nu}(x, im_\pi\hat{t})$ for a zero-momentum π^0 state defined in Eqs. (33) and (35). The only approximation is made in Eq. (42), which is based on large $m_\pi|x-y|$.

Using the 48I ensemble to calculate $\mathcal{F}$ and making this approximation, we obtained the long-distance part corresponding to $R_{\max} > 4$ fm

$$\begin{aligned}a_\mu(R_{\max}>4\text{ fm})\times 10^{10} &\approx a_\mu^{\pi^0\text{-exch}}(R_{\max}>4\text{ fm})\times 10^{10}\\ &= 2.00(11)_{\text{stat}}(28)_{\text{syst}},\end{aligned} \tag{47}$$

where we use the same subtracted infinite-volume QED weighting function as in the direct calculation. We estimate the relative systematic uncertainty from the approximation employed in Eq. (42) due to not including the charged loop contribution as

$$\frac{e^{-2m_\pi(4\text{ fm})}}{e^{-m_\pi(4\text{ fm})}} \approx 6\% \tag{48}$$

and the error from approximating the π^0 propagation direction to be along $x-y$ to be

$$\frac{0.5\text{ fm}}{4\text{ fm}} \approx 13\% \tag{49}$$

where we assume the typical separation for $|x-x'|$ and $|y-y'|$ to be 0.5 fm and $|x-y|$ to be 4 fm. Combining these two estimates in quadrature, we assigned 14% total systematic uncertainty for the long distance part ($R_{\max} > 4$ fm) contribution. Using the ratio between the connected and disconnected contributions as described in Eq. (28), we can also properly assign this contribution to the connected and disconnected diagrams. The results are shown in Table II with the labels "…$R_{\max} > 4$ fm."

D. Finite volume corrections

The long-distance part of the HLbL contribution usually suffers the most significant finite volume effects. However, the long-distance π^0 exchange contribution calculated in Sec. IV C is performed in infinite volume and is free of finite volume effects. Therefore, we only need to correct for the finite volume effects for the relatively short-distance region, where $R_{\max} < 4$ fm. These finite volume effects are expected to be quite small due to the constraint $R_{\max} < 4$ fm. The finite volume effects can be estimated with the "π^0-pole" contribution as defined in Ref. [20]. Similar to Refs. [21,66], we define the π^0 transition form factor in Euclidean space-time as

$$\begin{aligned}\mathcal{F}_{\mu,\nu}(x,p) &= \langle 0|TJ_\mu(x)J_\nu(0)|\pi^0(\vec{p})\rangle\\ &= \int\frac{d^4q_1}{(2\pi)^4}e^{iq_1\cdot x}\frac{-i}{4\pi^2F_\pi}\epsilon_{\mu,\nu,\rho,\sigma}q_{1\rho}q_{2\sigma}F_{\pi^0\gamma\gamma}(q_1^2,q_2^2)\end{aligned} \tag{50}$$

where $p=q_1+q_2$ and $p^2=-m_\pi^2$. We can convert the form factor into coordinate space via the following:

$$\int d^4u e^{ip\cdot u}\tilde{\mathcal{F}}_{\mu,\nu}(u,x,y) = \mathcal{F}_{\mu,\nu}(x-y,p). \tag{51}$$

The solution to the above condition is not unique. Based on the momentum space form factor $F_{\pi^0\gamma\gamma}(q_1^2,q_2^2)$ in Eq. (50), we obtain

TABLE V. Lattice calculation of the π^0-pole contribution using the LMD model. Note that this is not a lattice QCD calculation.

Label	Size	a^{-1}/GeV	$a_\mu(R_{\max} < 4\text{ fm}) \times 10^{10}$	$a_\mu(R_{\max} > 4\text{ fm}) \times 10^{10}$
Match	$48^3 \times 96$	1.73	5.19	0.22
Coarse	$24^3 \times 48$	0.865	4.65	0.20
Large	$64^3 \times 128$	0.865	4.18	2.34

$$\tilde{\mathcal{F}}_{\mu,\nu}(u,x,y) = \frac{i}{4\pi^2 F_\pi}\epsilon_{\mu,\nu,\rho,\sigma}\partial^x_\rho\partial^y_\sigma \int \frac{d^4q_1}{(2\pi)^4} e^{iq_1\cdot(x-u)} \times \int \frac{d^4q_2}{(2\pi)^4} e^{iq_2\cdot(y-u)} F_{\pi^0\gamma\gamma}(q_1^2, q_2^2). \tag{52}$$

Note this definition of the position space form factor is different from the inverse Fourier transformation of the Euclidean space hadronic matrix element $\mathcal{F}_{\mu,\nu}(x,p)$, since the on-shell condition $p^2 = -m_\pi^2$ for the physical π^0 state cannot be satisfied always in the inverse Fourier transformation. With the form factor defined above, we can construct the π^0-pole contribution to the hadronic four-point function:

$$\begin{aligned}\langle TJ_\mu(x)J_{\mu'}(x')J_\nu(y)J_{\nu'}(y')\rangle \approx \int d^4u \int d^4v D_{\pi^0}(u-v) \\ \times (\tilde{\mathcal{F}}_{\mu,\mu'}(u,x,x')\tilde{\mathcal{F}}_{\nu,\nu'}(v,y,y') \\ + \tilde{\mathcal{F}}_{\mu,\nu}(u,x,y)\tilde{\mathcal{F}}_{\mu',\nu'}(v,x',y') \\ + \tilde{\mathcal{F}}_{\mu,\nu'}(u,x,y')\tilde{\mathcal{F}}_{\mu',\nu}(v,x',y))\end{aligned} \tag{53}$$

where $D_{\pi^0}(x-y)$ is the infinite volume free scalar propagator with physical pion mass. In this calculation, we use the lowest meson dominance (LMD) model [38,67,68] for the π^0 transition form factors.

$$\begin{aligned}F_{\pi^0\gamma\gamma}(q_1^2,q_2^2) &\approx F^{\text{LMD}}_{\pi^0\gamma\gamma}(q_1^2,q_2^2) \\ &= F^{\text{VMD}}_{\pi^0\gamma\gamma}(q_1^2,q_2^2) + \frac{8\pi^2F_\pi^2}{3m_V^2} \\ &\quad\times (F^{\text{TE}}_{\pi^0\gamma\gamma}(q_1^2,q_2^2) - F^{\text{VMD}}_{\pi^0\gamma\gamma}(q_1^2,q_2^2)),\end{aligned} \tag{54}$$

where

$$F^{\text{VMD}}_{\pi^0\gamma\gamma}(q_1^2,q_2^2) = \frac{m_V^2}{q_1^2+m_V^2}\frac{m_V^2}{q_2^2+m_V^2} \tag{55}$$

$$F^{\text{TE}}_{\pi^0\gamma\gamma}(q_1^2,q_2^2) = \frac{m_V^2/2}{q_1^2+m_V^2} + \frac{m_V^2/2}{q_2^2+m_V^2}. \tag{56}$$

The parameters used in the calculation are $m_\pi = 134.9766$ MeV, $F_\pi = 92$ MeV, $m_V = 770$ MeV. We discretize the model and calculate it with lattices of different sizes using the same subtracted infinite volume QED weighting as the direct calculation. The results are given in Table V. Note the physical size of the "match" and "coarse" lattices are the same as the 48I ensemble, which we used to perform our main lattice QCD calculation. The spatial size is $L = 5.5$ fm. The "large" lattice has the same lattice spacing as the "coarse" lattice but has a much larger physical size, $L = 16.4$ fm. We use the difference between the "large" and the "coarse" results of $a_\mu(R_{\max} < 4\text{ fm}) \times 10^{10}$ as the finite volume correction. Comparing the results of "match" and "coarse," we estimate the uncertainty due to the nonzero lattice spacing effects of this model lattice calculation can be about 12%. Combined with the additional 20% uncertainty due to the inaccuracy of the model itself (and potential finite volume corrections of other heavier intermediate states), we obtain our final estimate of the finite volume correction:

$$a_\mu^{\text{FV-corr}}(R_{\max} < 4\text{ fm}) \times 10^{10} = -0.47(11)_{\text{syst}}. \tag{57}$$

Similar to the long-distance π^0-exchange contribution, we use the ratio between the connected and disconnected contributions as described in Eq. (28) to assign this contribution to the connected and disconnected diagrams. The results are shown in Table II as "48I light con FV-corr," "48I light discon FV-corr," and "48I light FV-corr."

Also, note that we can calculate the long-distance π^0-pole contribution using this LMD model. In Table V, we also list the contribution to the region $R_{\max} > 4$ fm. Using the LMD model results calculated with the large lattice, we obtain

$$a_\mu^{\pi^0\text{-pole;LMD}}(R_{\max} > 4\text{ fm}) \times 10^{10} = 2.34. \tag{58}$$

This result agrees with the long-distance π^0-exchange contribution calculated with π^0 transition form factors from the previously described lattice QCD calculation and long-distance approximation.

E. Pion mass extrapolation

While the calculation is performed very near the physical pion mass, there is a slight mistuning of the lattice parameters which leads to a slightly heavier $m_\pi = 139$ MeV compared to the physical pion mass $m_\pi = 134.9766$ MeV. We correct this small difference using the 32D and 24DH ensembles. These two ensembles have the same lattice spacing but different pion masses. The results of these two ensembles are listed in Table VI. Note that for the

TABLE VI. Study of the pion mass dependence using the 32D and 24DH ensembles. For the 32D (physical pion mass ensemble) results, we apply the 48I long-distance π^0-exchange contribution in the $R_{\text{max}} > 4$ fm region. For the 24DH ensemble ($m_\pi = 341$ MeV), we assume the contribution is negligible in the $R_{\text{max}} > 4$ fm region.

Name	R_{max} limit	$a_\mu(32\text{D})\times 10^{10}$	$a_\mu(24\text{DH})\times 10^{10}$
Con	2 fm	$8.17\ (0.32)_{\text{stat}}$	$8.29\ (0.10)_{\text{stat}}$
Con	4 fm	$21.29\ (3.37)_{\text{stat}}$	$12.35\ (0.24)_{\text{stat}}$
Con	∞	$28.84\ (3.39)_{\text{stat}}$	$12.35\ (0.24)_{\text{stat}}$
No-pion	2 fm	$3.91\ (0.63)_{\text{stat}}$	$4.18\ (0.57)_{\text{stat}}$
No-pion	4 fm	$4.96\ (4.46)_{\text{stat}}$	$6.74\ (4.18)_{\text{stat}}$
Discon	2 fm	$-2.10\ (0.59)_{\text{stat}}$	$-1.91\ (0.55)_{\text{stat}}$
Discon	4 fm	$-10.70\ (3.84)_{\text{stat}}$	$-2.34\ (4.18)_{\text{stat}}$
Discon	∞	$-16.25\ (3.84)_{\text{stat}}$	$-2.34\ (4.18)_{\text{stat}}$
Discon hybrid-2 fm	4 fm	$-11.74\ (2.52)_{\text{stat}}$	$-4.90\ (0.54)_{\text{stat}}$
Discon hybrid-2 fm	∞	$-17.30\ (2.53)_{\text{stat}}$	$-4.90\ (0.54)_{\text{stat}}$
Total	2 fm	$6.07\ (0.66)_{\text{stat}}$	$6.38\ (0.57)_{\text{stat}}$
Total	4 fm	$10.59\ (4.97)_{\text{stat}}$	$10.01\ (4.18)_{\text{stat}}$
Total	∞	$12.59\ (4.98)_{\text{stat}}$	$10.01\ (4.18)_{\text{stat}}$
Total hybrid-2 fm	4 fm	$9.55\ (1.12)_{\text{stat}}$	$7.45\ (0.59)_{\text{stat}}$
Total hybrid-2 fm	∞	$11.55\ (1.12)_{\text{stat}}$	$7.45\ (0.59)_{\text{stat}}$

long-distance contribution ($R_{\text{max}} > 4$ fm) for the 32D physical pion mass ensemble, we use the same long-distance π^0-exchange contribution calculated with ensemble 48I as described in Sec. IV C. Similar to the 48I calculation, we calculate the "no-pion" contribution and obtain the "hybrid-2 fm" results for the "discon" and "total" results. To reduce the statistical error, we use the "hybrid-2 fm" results to calculate the pion mass correction. To obtain the pion mass correction to our main 48I results, we assume the following pion mass dependence for the "no-pion" contribution:

$$a_\mu^{\text{no-pion}}(m_\pi) = C_1 + C_2 m_\pi^2. \tag{59}$$

Due to the pion pole piece in the quark-connected diagram, we assume a more singular pion mass dependence for the "con" contribution

$$a_\mu^{\text{con}}(m_\pi) = C_1 + \frac{C_2}{m_\pi^2}. \tag{60}$$

The disconnected diagram contribution can be obtained as a combination of the "con" and "no-pion" contribution as given in Eqs. (31)[(32)].

The fitting form in Eq. (60) (plus an additional m_π^2 term) was used for the chiral extrapolation of the connected diagram in Ref. [48] and seems to provide the most accurate description of the connected diagram's mass dependence. The correction from the chiral extrapolation is $0.35(7) \times 10^{-10}$ with the above fitting form. In Ref. [26], the π^0-pole contribution is calculated to behave as $C_1 + C_2 \log^2(m_\pi^2)$, If we estimate the pion mass correction with this form instead, the size of the correction is $0.20(4) \times 10^{-10}$. In Ref. [69], the HLbL is calculated with chiral effective theory, we have calculated the pion mass dependence with Eq. (13) of this reference. The shift of a_μ due to the pion mass change from the 139 MeV used in the lattice calculation to the physical point 135 MeV is 0.25×10^{-10}. Here, we do not include the correction to the charged pion loop contribution of a_μ due to the pion mass shift, as the charged pion loop contribution are significantly reduced compared with the scalar QED estimate due to the pion dressing [70–72]. We, therefore, estimate a 50% systematic uncertainty to these corrections to account for possible inaccuracies of the empirical chiral extrapolations, plus any systematic effects in obtaining the 32D and 24DH results, including the effects caused by the hybrid method used to calculate the long-distance part of the disconnected diagrams, the discretization effects, the finite volume effects, and so on. The final results for the correction due to the slight mismatch of the pion mass is

$$\begin{aligned} a_\mu^{m_\pi\text{-corr}} \times 10^{10} &= (a_\mu(m_\pi = 135\ \text{MeV}) \\ &\quad - a_\mu(m_\pi = 139\ \text{MeV})) \times 10^{10} \\ &= 0.35(0.07)_{\text{stat}}(0.17)_{\text{syst}}. \end{aligned} \tag{61}$$

We also show the results in Table II as "48I light con m_π-corr," "48I light discon m_π-corr," and "48I light m_π-corr."

F. Continuum limit extrapolation

In our previous work [24], we used finite-volume lattices for the entire calculation, including QED. The QED$_L$ scheme was used for the photon propagators, and sizable discretization effects were observed. We took the continuum limit with the 48I and 64I ensembles. These two ensembles have different lattice spacings but all other properties are almost identical. They have the same gauge and fermion actions, and almost the same pion mass and volume in physical units.

We used the results from these two ensembles to perform the continuum extrapolation. The continuum limit value is 30(12)% higher compared to the value on the 48I ensemble for the connected piece and 58(27)% higher for the disconnected piece. The numbers in parentheses are statistical uncertainties.

In this work, we have mainly used the 48I ensemble to perform the calculation with the infinite volume, continuum QED weighting function described in Ref. [46]. Compared with QED_L, the infinite volume QED weighting function reduces the finite volume effects from power-law to exponential.

One may expect similar discretization effects for these two calculations since they should be the same in the large volume limit and only differ by finite volume effects. However, there are two reasons that the discretization errors in the current work should be much smaller. First, the infinite volume QED weighting function is calculated in the continuum with a semianalytic method, which eliminates the discretization errors in the QED_L weighting function which is calculated on a discrete lattice. Second, and more importantly, we apply the subtraction scheme as described in Ref. [46] and repeated in Eq. (12). In a test calculation of the leptonic light-by-light contribution to the muon $g-2$, we found about a factor of 5 reduction in the discretization error after this subtraction is applied. We expect a similar reduction in discretization error in the hadronic case, and this is indeed the case in our calculation of the strange quark connected diagrams.

The strange quark connected contribution is shown in Fig. 9. Compared with the light quark, due to the heavier strange quark mass, the statistical noise in the long-distance region is very small. The overall signal-to-noise ratio is much better than the light quark case which allows a precise continuum limit extrapolation. As is shown in the figure, the limit is 7.9(2.6)% higher than the 48I results. The continuum limit is obtained by performing an $\mathcal{O}(a^2)$ extrapolation to $a \to 0$,

$$a_\mu(a^2) = C_1 + C_2 a^2. \tag{62}$$

Compared with the observed ~30% discretization error in the QED_L calculation of the light quark connected diagrams, there is indeed a significant reduction in the relative discretization error with the subtracted infinite volume weighting function, despite the heavier strange quark mass, which usually leads to larger discretization errors.

The study of the continuum limit of the strange quark connected diagrams strongly suggests the light quark connected diagrams, in particular in the relatively short distance region where we performed a reliable continuum extrapolation for the strange quark connected diagrams, is under 8%. We also have the same 64I dataset for the light quark connected diagram. We have listed the comparison in Table VII. The results from the 64I ensemble are statistically consistent with the 48I ensemble. Unfortunately, the statistical error for 64I is relatively larger due to the absence of the improvement we made for the new 48I calculation. We cannot constrain the continuum extrapolation for the light quark connected diagram better than the 8% estimate above based on the strange quark connected results.

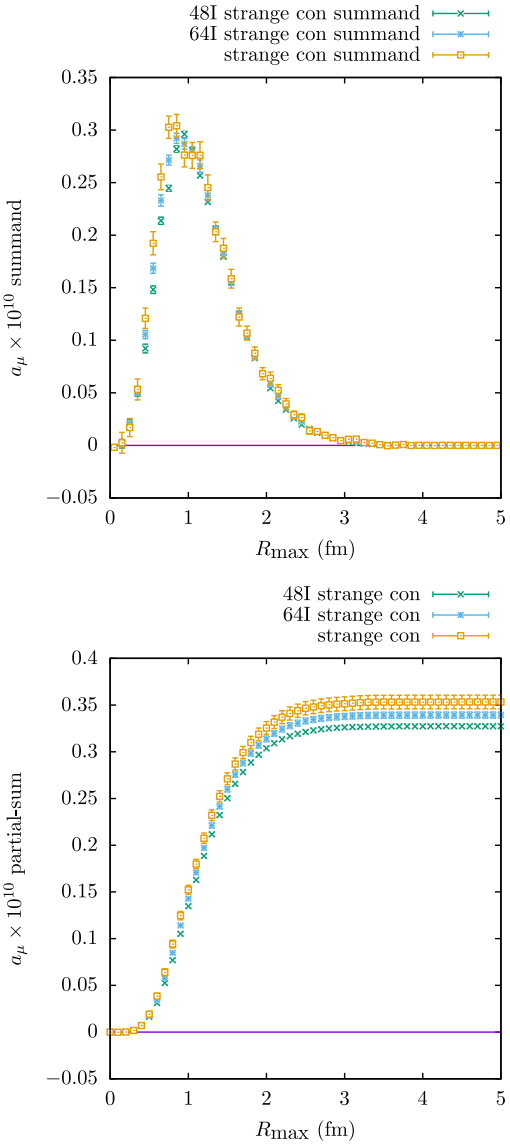

FIG. 9. Strange quark connected part of a_μ^{HLbL} (lower panel). Continuum limit (upper curve) and finite lattice spacing results on 48I and 64I ensembles. Corresponding summands (upper panel).

In the long distance (large R_{max}) region, the contributions are mostly coming from the π^0-exchange contribution. As can be seen from Eq. (42), the hadronic four-point function in the HLbL diagrams in the long-distance part can be approximated by the product of two such transition form factors. Therefore, the discretization effects of the direct calculation of the four-point function in the long distance region will be similar to the discretization effects of the calculation of the square of the transition form factor. In the $\pi^0 \to e^+e^-$ calculation of Ref. [73], this relevant $\pi^0 \to \gamma\gamma$ transition

TABLE VII. The last column is the percent correction to obtain the continuum limit relative to the value of the 48I ensemble. The values in parentheses are the statistical uncertainty of the corresponding quantity.

Observable	48I	64I	Percentage correction
$a_\mu^{\rm con}(R_{\rm max} < 1.0\ {\rm fm}) \times 10^{10}$	1.27(0.02)	1.32(0.05)	9.2(8.6)
$a_\mu^{\rm con}(R_{\rm max} < 1.5\ {\rm fm}) \times 10^{10}$	3.92(0.05)	4.04(0.23)	7.0(12.6)
$a_\mu^{\rm con}(R_{\rm max} < 2.0\ {\rm fm}) \times 10^{10}$	7.24(0.15)	7.19(0.66)	−1.4(20.0)
$a_\mu^{\rm con}(R_{\rm max} < 2.5\ {\rm fm}) \times 10^{10}$	10.64(0.31)	9.61(1.40)	−20.8(29.2)

form factor is studied with the same 48I ensemble as this calculation. In addition, the continuum limit is calculated with a parallel 64I ensemble calculation. We quote the corrections obtained in the calculation in Table VIII. Note that the correction is zero consistent given the statistical uncertainty. In Fig. 4 of Ref. [73], the partial sum of these quantities for both 48I and 64I are plotted. More statistically precise agreement is observed at smaller time separation of the two electromagnetic vector currents.

For the light quark disconnected diagrams, we again separately discuss the short and long distance regions. In Fig. 5, we observe that in the short distance region ($R_{\rm max} \lesssim 2$ fm), the disconnected diagram contribution is much smaller than the connected contribution. This is expected as the disconnected diagrams involve two quark loops and the exchange of at least two gluons. Therefore, the disconnected diagrams are suppressed by $\mathcal{O}(\alpha_s^2)$ and $1/N_c$ relative to the connected diagrams. Due to the smallness of the contributions from the short-distance disconnected diagrams, we expect that the same reasoning applies to the discretization effects.

For the long distance region, we again have Eq. (28), which mandates the relationship with the connected diagrams, even for nonzero lattice spacing and finite volume (so long that the lattice is large enough to contain the correlation function). Therefore, we expect the long distance part of the disconnected diagrams to have the same relative discretization effects as the connected diagrams and also the combined total. Note that the situation is different from the Mainz group's work in Refs. [47,48]. While the argument presented here should also apply to the hadronic function in their calculation, the different QED kernels (due to the subtraction scheme of the QED kernel and the choice of $x_{\rm ref}$) used for the connected and disconnected diagrams lead to different shapes of the summands and also different discretization errors.

Without a 64I ensemble calculation of similar precision, the continuum limit cannot be reliably taken. However, based on the evidence presented above, in particular the size of the correction in the strange quark connected diagrams, we estimate an 8% uncertainty from nonzero lattice spacing for the contributions from the light quark connected, disconnected, and total contributions, and the strange quark disconnected diagrams. The corrections for light quark are shown in Table II as "48I light con a^2-corr," "48I light discon a^2-corr," and "48I light a^2-corr." The corrections for the strange quark are shown in Table IV as "48I strange con a^2-corr," "48I strange discon a^2-corr," and "48I strange a^2-corr."

TABLE VIII. Percent correction to obtain the continuum limit relative to the value computed on the 48I ensemble in the $\pi^0 \to e^+e^-$ calculation in Ref. [73]. The values in parentheses are the statistical uncertainty of the corresponding quantity. The square of the amplitude is used to estimate the lattice spacing error of the long-distance π^0-exchange contribution to the muon $g-2$ in this work.

Observable	Percentage correction
$({\rm Im}\mathcal{A})^2$	−11.4(11.6)%
$({\rm Re}\mathcal{A})^2$	−16.8(15.8)%

G. Subleading disconnected diagrams

So far, our discussions have centered on the first two diagrams in Fig. 2. The remaining diagrams, which are expected to be small due to the suppression by flavor SU(3) and quark electric charge factors, are not yet included. In our earlier work [24], we have already calculated the third diagram in Fig. 2, which is expected to be the largest within the remaining the subleading disconnected diagrams based on the flavor SU(3) and quark electric charge factor counting. To estimate the contribution from this diagram, we employ the same subtracted infinite volume QED weighting function and the 24D ensemble for the quark

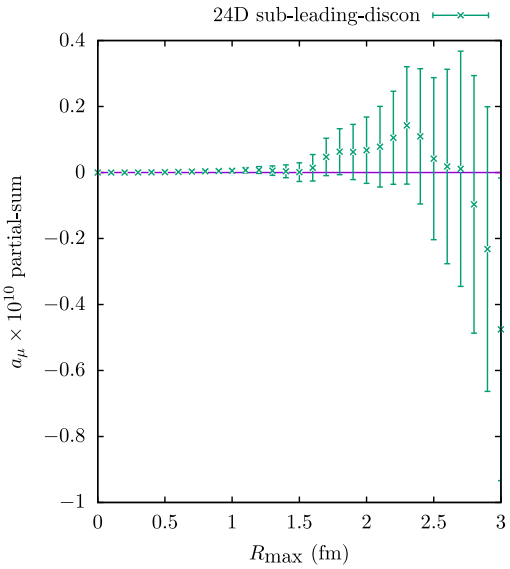

FIG. 10. Subleading disconnected diagrams computed on the 24D ensemble [24].

TABLE IX. Summary of final results. Values are different contributions to $a_\mu \times 10^{10}$ where $a_\mu = (g_\mu - 2)/2$. The numbers in the square bracket (except references) are the statistical and systematic uncertainty combined in quadrature. The "strange discon" contribution includes disconnected diagrams where one or two loops are strange quark loops. The tag "hybrid-" indicates the same quantity obtained using the hybrid approach as described in Secs. IV A and IV B. The result for "total hybrid-2.5 fm" is used as our final result.

Contribution	$a_\mu \times 10^{10}$
Light con	$25.70\ (1.33)_{\rm stat}(1.99)_{\rm syst}[2.39]$
Light discon	$-12.71\ (1.87)_{\rm stat}(1.17)_{\rm syst}[2.20]$
Light discon hybrid-2.5 fm	$-13.50\ (1.36)_{\rm stat}(1.21)_{\rm syst}[1.82]$
Light discon hybrid-2 fm	$-13.37\ (1.29)_{\rm stat}(1.46)_{\rm syst}[1.95]$
Light total	$12.99\ (2.11)_{\rm stat}(0.90)_{\rm syst}[2.29]$
Light total hybrid-2.5 fm	$12.20\ (1.01)_{\rm stat}(0.95)_{\rm syst}[1.38]$
Light total hybrid-2 fm	$12.33\ (0.90)_{\rm stat}(1.25)_{\rm syst}[1.55]$
Strange con	$0.35\ (0.01)_{\rm stat}$
Strange discon	$-0.38\ (0.61)_{\rm stat}(0.03)_{\rm syst}[0.61]$
Strange discon hybrid-2.5 fm	$-0.36\ (0.22)_{\rm stat}(0.03)_{\rm syst}[0.22]$
Strange discon hybrid-2 fm	$-0.28\ (0.12)_{\rm stat}(0.04)_{\rm syst}[0.13]$
Strange total	$-0.03\ (0.61)_{\rm stat}(0.03)_{\rm syst}[0.61]$
Strange total hybrid-2.5 fm	$-0.00\ (0.22)_{\rm stat}(0.03)_{\rm syst}[0.23]$
Strange total hybrid-2 fm	$0.07\ (0.12)_{\rm stat}(0.04)_{\rm syst}[0.13]$
Subleading discon	$0.00\ (0.07)_{\rm syst}$ [48]
Charm con	$0.31\ (0.04)_{\rm syst}$ [49]
Charm discon	$-0.03\ (0.02)_{\rm syst}$ [49]
Charm total	$0.28\ (0.05)_{\rm syst}$ [49]
Con	$26.36\ (1.33)_{\rm stat}(1.99)_{\rm syst}[2.39]$
Discon	$-13.12\ (2.30)_{\rm stat}(1.18)_{\rm syst}[2.59]$
Discon hybrid-2.5 fm	$-13.89\ (1.47)_{\rm stat}(1.22)_{\rm syst}[1.91]$
Discon hybrid-2 fm	$-13.68\ (1.35)_{\rm stat}(1.47)_{\rm syst}[1.99]$
Total	$13.24\ (2.53)_{\rm stat}(0.90)_{\rm syst}[2.68]$
Total hybrid-2.5 fm	$12.47\ (1.15)_{\rm stat}(0.95)_{\rm syst}[1.49]$
Total hybrid-2 fm	$12.68\ (0.98)_{\rm stat}(1.26)_{\rm syst}[1.59]$

loops. The result, shown in Fig. 10, is zero consistent, and we estimate this contribution to be $0.0(0.5) \times 10^{-10}$.

In the more recent work by the Mainz group [48], all the subleading diagrams have been calculated. The result is still zero consistent but a more stringent bound is obtained. Therefore, in this work, we use their result to account for the contribution from all the subleading disconnected diagrams. The value is shown in Table IX as "subleading discon."

H. Charm quark contributions

The charm quark contribution is also expected to be very small due its heavy mass relative to the light quark and the strange quark. In the 2020 white paper [5], its contribution is included as $0.3(0.1) \times 10^{-10}$, calculated based on perturbation theory and consideration of charm meson resonances [23]. The value is similar to the strange quark connected diagram contribution due to the heavier mass of the charm quark and larger electric charge. In a recent work by the Mainz group [49], the charm quark contribution is calculated with lattice QCD, including both the charm quark connected and disconnected diagrams. The result for the total charm quark contribution is $0.28(0.05) \times 10^{-10}$, where the uncertainty is mostly due to the systematic effects from modeling the lattice spacing and M_{η_c} dependence. In this work, we use this more recent lattice calculated result to account for the contribution from the charm quark. The values are shown in Table IX as "charm con," "charm discon," "charm."

V. CONCLUSION

We summarized all the results discussed above in Tables II, IV, and IX. Adding all the individual contributions and corrections, we obtain our final result for the HLbL contribution to the muon $g-2$

$$a_\mu^{\rm HLbL} \times 10^{10} = 12.47(1.15)_{\rm stat}(0.95)_{\rm syst}[1.49], \quad (63)$$

where the systematic errors were added in quadrature. We also give the HLbL contributions to the muon $g-2$ from the connected and disconnected pieces separately

$$a_\mu^{\rm HLbL,con} \times 10^{10} = 26.36(1.33)_{\rm stat}(1.99)_{\rm syst}[2.39], \quad (64)$$

$$a_\mu^{\rm HLbL,discon} \times 10^{10} = -13.89(1.47)_{\rm stat}(1.22)_{\rm syst}[1.91]. \quad (65)$$

Numbers in square brackets denote total errors, combining the statistical uncertainty ("stat") and systematic ones ("sys") in quadrature.

TABLE X. Comparison of this work with our previous $\rm QED_L$ results [24] plus the charm quark contribution from [5,23]. The field "all con" includes all connected diagram contributions, including the charm quark. The field "all discon" includes all the disconnected diagram contributions, including the subleading disconnected diagrams and disconnected diagrams including charm quarks. The fields "all con diff," "all discon diff," "total diff" shows the difference obtained by subtracting the $\rm QED_L$ results from the new results presented in this work. The statistical and systematic uncertainties of the two works are almost independent. We therefore add them in quadrature for the difference. The numbers in the square bracket are the statistical and systematic uncertainty combined in quadrature.

	$a_\mu \times 10^{10}$
All con $\rm QED_L$	$24.46\ (2.35)_{\rm stat}(5.11)_{\rm syst}[5.62]$
All con diff	$1.90\ (2.76)_{\rm stat}(5.48)_{\rm syst}[6.14]$
All discon $\rm QED_L$	$-16.45\ (2.09)_{\rm stat}(3.99)_{\rm syst}[4.50]$
All discon diff	$2.56\ (2.57)_{\rm stat}(4.17)_{\rm syst}[4.90]$
Total $\rm QED_L$	$8.17\ (3.03)_{\rm stat}(1.77)_{\rm syst}[3.51]$
Total diff	$4.30\ (3.25)_{\rm stat}(2.01)_{\rm syst}[3.82]$

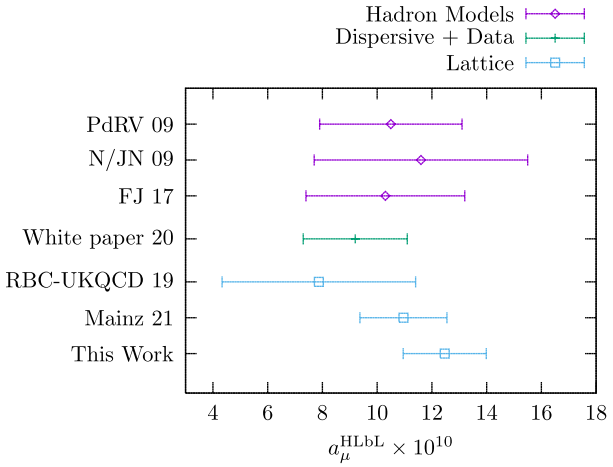

FIG. 11. Comparison of our result with values in the literature. The hadronic model values are from Refs. [26–29]. The dispersive data driven result is compiled in Ref. [5]. The lattice results include Refs. [24,48,49] and this work.

Here, we summarize techniques used in this calculation that we believe are important to obtain the precision for HLbL scattering at the physical pion mass:

(i) The subtracted infinite volume QED weighting function developed in our previous work [46].
(ii) Use all combinations of the point source propagators to calculate the HLbL diagrams as described in Sec. III.
(iii) The adaptive sampling scheme used for the disconnected diagram calculation as described in Sec. III.
(iv) The rearrangement of the connected and disconnected diagrams in Eqs. (29), (32) based on Eq. (28).
(v) The AMA method [58] and efficient GPU solver for MDWF propagators from Grid and GPT.

We can compare these results with our previous work [24] based on the finite volume QED_L formulation. The comparison is summarized in Table X. We can see that the results for both the connected and disconnected diagrams are in good agreement. For the total, the current result is 1.12 standard deviations higher than the previous results, possibly due to a slightly larger statistical fluctuation. We also compare the final result in this work with the existing literature in Fig. 11. The new result is consistent with previous determinations.

ACKNOWLEDGMENTS

We thank our RBC and UKQCD collaborators for helpful discussions and critical software and hardware support. T. B. and L. J. have been supported under US DOE Grant No. DE-SC0010339. L. J. is also supported by U.S. DOE Office of Science Early Career Award No. DE-SC0021147. N. C. is supported by US DOE Grant No. DE-SC0011941. M. H. is supported by Japan Grants-in-Aid for Scientific Research, No. 20K03926. T. I., C. J., and C. L. were supported in part by U.S. DOE Contract No. DESC0012704(BNL). T. I. and C. J. were supported in part by the Scientific Discovery through Advanced Computing (SciDAC) program LAB 22-2580. T. I. is also supported by the Department of Energy, Laboratory Directed Research and Development (LDRD No. 23-051) of BNL and RIKEN BNL Research Center, and by JSPS KAKENHI under Grants No. JP26400261, No. JP17H02906. C. L. has been supported by a DOE Office of Science Early Career Award. We developed the computational code used for this work based on the Columbia Physics System (CPS), Grid, GPT, and Qlattice. Computations were performed mainly under the ALCC Program of the US DOE on the SUMMIT computer at the Oak Ridge Leadership Computing Facility, a DOE Office of Science Facility supported under Contract No. DE-AC05-00OR22725. These calculations used gauge configurations and propagators created using resources of the Argonne Leadership Computing Facility, which is a DOE Office of Science User Facility supported under Contract No. DE-AC02-06CH11357. We also acknowledge computer resources at the Oakforest-PACS supercomputer system at Tokyo University, partly through the HPCI System Research Project (hp180151, hp190137), the BNL SDCC computer clusters at Brookhaven National Lab as well as computing resources provided through USQCD at Brookhaven and Jefferson National Labs.

APPENDIX A: NOTATION

We use S_μ and G to denote free muon and photon propagators:

$$S_\mu(x,y) = \int \frac{d^4p}{(2\pi)^4} \frac{1}{i\not{p} + m} e^{ip\cdot(x-y)} \tag{A1}$$

$$= (-\not{\partial}_x + m) \int \frac{d^4p}{(2\pi)^4} \frac{1}{p^2+m^2} e^{ip\cdot(x-y)}, \tag{A2}$$

$$G(x,y) = \int \frac{d^4p}{(2\pi)^4} \frac{1}{p^2} e^{ip\cdot(x-y)} \tag{A3}$$

$$= \frac{1}{4\pi^2} \frac{1}{(x-y)^2}. \tag{A4}$$

The γ_μ matrices satisfy the Euclidean space-time metric

$$\gamma_\mu\gamma_\nu + \gamma_\nu\gamma_\mu = 2\delta_{\mu,\nu}, \tag{A5}$$

and

$$\gamma_5 = \gamma_x\gamma_y\gamma_z\gamma_t. \tag{A6}$$

APPENDIX B: π^0 LONG-DISTANCE CONTRIBUTION

In Eq. (42), we replaced the QCD, Euclidean space-time, four-current connected Green's function with the product of two amplitudes, each coupling a pair of currents to an on-shell π^0. These two amplitudes are joined by a pion propagator and all amplitudes are expressed in position space, so they can be directly inserted in our standard position-space evaluation of the HLbL amplitude. Since the final expression involves two independent factors evaluating the $\pi\gamma\gamma$ coupling which are connected by an analytic, position-space pion propagator, this QCD part of the HLbL amplitude can be evaluated in a "QCD volume" of arbitrary size. In particular, this volume could be much larger than that of the gauge configurations used to compute each $\pi\gamma\gamma$ vertex function. Here we work out a concrete derivation of this formula that can be used to evaluate the long-distance part of the π^0 exchange contribution to the leading order in $1/L$. We leave open the possibility that this approach could be developed further to systematically capture terms falling with higher powers of $1/L$ if the large volume π^0 contribution is expressed as a power series in $1/L^n$ where L is the size of the QCD volume. We assume the QED volume to be infinite.

We begin with the Euclidean-space Green's function defined in Eq. (15)

$$6e^4\mathcal{H}_{\mu',\mu,\nu',\nu}(x',x,y',y) = \langle T(J_{\mu'}(x')J_{\mu}(x)J_{\nu'}(y')J_{\nu}(y))\rangle. \tag{B1}$$

We will choose x' and x close to each other as are y' and y. However, we will assume that the (x',x) pair is far from the (y',y) pair. Define

$$\tilde{x} = x' - x, \tag{B2}$$

$$\tilde{y} = y' - y. \tag{B3}$$

Since Euclidean space-time is rotational invariant, without loss of generality, we can choose $x-y$ to be along the Euclidean time direction, with $x-y=(t,\vec{0})$ and $t>0$.

We now follow the usual steps to obtain a variant of the Källen-Lehman representation of the amplitude but keep only the single π^0 intermediate state since, as the lightest particle, its exchange will dominate this Green's function when x and y are far separated

$$\begin{aligned} &6e^4\mathcal{H}^{\pi^0}_{\mu',\mu,\nu',\nu}(x',x,y',y) \\ &= \int \frac{d^3p}{(2\pi)^3}\frac{1}{2E_{\pi,\vec{p}}}\langle 0|T(J_{\mu'}(x')J_{\mu}(x))|\pi^0(\vec{p})\rangle \\ &\quad\times\langle \pi^0(\vec{p})|T(J_{\nu'}(y')J_{\nu}(y))|0\rangle, \end{aligned} \tag{B4}$$

where the superscript π^0 indicates that only the π^0 contribution to $\mathcal{H}$ is represented.

Next we use four-dimensional translational invariance to remove the variables x and y from the two current-current-π^0 amplitudes. We will also replace these two $O(4)$-covariant current-current-π^0 amplitudes by functions of the four momentum $p=(iE_{\pi,\vec{p}},\vec{p})$. Given the factors of $\exp(ip\cdot x)$ and $\exp(-ip\cdot y)$ which appear, we can then replace the four vector p_μ by $-i\partial/\partial x_\mu$ or $i\partial/\partial y_\mu$ as needed. For example,

$$\begin{aligned} \langle 0|T(J_{\mu'}(x')J_{\mu}(x))|\pi^0(\vec{p})\rangle &= \langle 0|T(J_{\mu'}(\tilde{x})J_{\mu}(0))|\pi^0(\vec{p})\rangle e^{ip\cdot x} \\ &= \mathcal{F}_{\mu',\mu}(\tilde{x},p)e^{ip\cdot x} \\ &= \mathcal{F}_{\mu',\mu}\left(\tilde{x},-i\frac{\partial}{\partial x}\right)e^{ip\cdot x}. \end{aligned} \tag{B5}$$

where the definition of the π^0 transition form factors follows Eq. (33).

Using this approach to remove the explicit dependence of the two amplitudes on p_μ, we can then perform the final step of the usual Källen-Lehman derivation and introduce the free pion propagator

$$\int \frac{d^3p}{(2\pi)^3}\frac{1}{2E_{\pi,\vec{p}}}e^{ip\cdot(x-y)} = \int \frac{d^3p}{(2\pi)^3}\frac{1}{2E_{\pi,\vec{p}}}e^{i\vec{p}\cdot(\vec{x}-\vec{y})}e^{-E_{\pi,\vec{p}}(x_t-y_t)} \tag{B6}$$

$$= \int \frac{d^4p}{(2\pi)^4}\frac{e^{ip\cdot(x-y)}}{p^2+m_\pi^2} \tag{B7}$$

$$= D_{\pi^0}(x-y) \tag{B8}$$

where $D_{\pi^0}(x-y)$ is the free Euclidean-space propagator for a scalar particle of mass m_π.

We can then rewrite Eq. (B4) in terms of $\mathcal{F}$ and D_{π^0} to obtain the result

$$\begin{aligned} 6e^4\mathcal{H}^{\pi^0}_{\mu',\mu,\nu',\nu}(x',x,y',y) &= \mathcal{F}_{\mu',\mu}\left(\tilde{x},-i\frac{\partial}{\partial x_\mu}\right)\mathcal{F}_{\nu',\nu}\left(\tilde{y},-i\frac{\partial}{\partial y_\mu}\right) \\ &\quad\times D_{\pi^0}(x-y). \end{aligned} \tag{B9}$$

At this step, we have made explicit the $O(4)$-covariance of the right-hand side of the equation. So this equation should hold for an arbitrary orientation of $x-y$.

So far all of the steps taken have been exact. We expect the quantity computed, the contribution of a single pion exchange, to dominate the long distance limit in which $|x-y|$ is large, i.e., $|x-y|\gtrsim L$. Now we will evaluate the derivatives with respect to x and y which appear in these equations but keep only the leading term in an expansion in powers of $1/L$. For example, to leading order in $1/|x-y|$

$$\prod_{i=1}^{N}\left(\frac{\partial}{\partial x_{\rho_i}}\right)D_{\pi^0}(x-y) = \prod_{i=1}^{N}\left(\frac{\partial}{\partial x_{\rho_i}}\right)\frac{ce^{-m_\pi|x-y|}}{|x-y|^{3/2}} \tag{B10}$$

$$\approx \prod_{i=1}^{N} \left(-m_\pi \frac{(x-y)_{\rho_i}}{|x-y|} \right) \frac{c e^{-m_\pi |x-y|}}{|x-y|^{3/2}}, \tag{B11}$$

where the relation holds for arbitrary N and ρ_i labels the component of x appearing in the i^{th} derivative in the product of N derivatives. Here we use the large distance behavior of $D_{\pi^0}(x-y)$

$$D_{\pi^0}(x-y) \approx \frac{c e^{-m_\pi |x-y|}}{|x-y|^{3/2}}. \tag{B12}$$

Introducing this approximation into Eq. (B9), we obtain

$$6e^4 \mathcal{H}^{\pi^0}_{\mu',\mu,\nu',\nu}(x',x,y',y) \approx \mathcal{F}_{\mu',\mu}(\tilde{x}, im_\pi \hat{n}) \mathcal{F}_{\nu',\nu}(\tilde{y}, -im_\pi \hat{n}) \times D_{\pi^0}(x-y). \tag{B13}$$

where $\hat{n}_\mu$ is the Euclidean unit vector $(x-y)_\mu/|x-y|$. This is finally the equation of interest, Eq. (42), which appeared earlier. Since the two quantities expressed in terms of the form factor $\mathcal{F}$ can be evaluated from independent lattice QCD ensemble averages, the expression on the right hand side of Eq. (B13) can be evaluated from a standard lattice QCD ensemble average followed by an $O(4)$ rotation as defined in Eq. (43), which we repeat here

$$\mathcal{F}_{\mu',\mu}(\tilde{x}, im_\pi \hat{n}) = \Lambda_{\mu',\rho'} \Lambda_{\mu,\rho} \mathcal{F}_{\rho',\rho}(\tilde{x}', im_\pi \hat{t}), \tag{B14}$$

The $O(4)$ rotation matrix $\Lambda = \Lambda(\hat{n})$ and Euclidean space-time coordinate $\tilde{x}'$ satisfy

$$\delta_{\mu,\nu} = \Lambda_{\mu,\mu'} \Lambda_{\nu,\nu'} \delta_{\mu',\nu'}, \tag{B15}$$

$$\hat{n}_\mu = \Lambda_{\mu,\mu'} \hat{t}_{\mu'}, \tag{B16}$$

$$\tilde{x}_\mu = \Lambda_{\mu,\mu'} \tilde{x}'_{\mu'}. \tag{B17}$$

The rotated form factor $\mathcal{F}_{\rho',\rho}(\tilde{x}', im_\pi \hat{t})$ follows the definition Eq. (B5) or Eq. (33) with zero momentum π^0 state

$$\begin{aligned} &\mathcal{F}_{\rho',\rho}(\tilde{x}', im_\pi \hat{t}) \\ &= \langle 0 | T J_{\rho'}(\tilde{x}') J_\rho(0) | \pi^0(\vec{p} = \vec{0}) \rangle \\ &= \sqrt{2m_\pi L^3} \lim_{t_{\rm tsep} \to +\infty} \frac{\langle T J_{\rho'}(\tilde{x}') J_\rho(0) \pi^0(-t_{\rm sep}) \rangle}{\sqrt{\langle T \pi^0(t_{\rm sep}) \pi^0(-t_{\rm sep}) \rangle}}, \end{aligned} \tag{B18}$$

where $\pi^0(t)$ is a zero momentum π^0 interpolating operator. We use Coulomb fixed gauge wall source pion operator in our numerical lattice calculation. The other factor $\mathcal{F}_{\nu',\nu}(\tilde{y}, -im_\pi \hat{n})$ can be calculated similarly.

The above procedure allows a direct calculation of the π^0 contribution to the long distance part the HLbL amplitude without relying on any parametrization or modeling of the π^0 transition form factor.

In this calculation, we employ this long-distance π^0-exchange approximation in the following region:

$$R_{\rm max} = \max(|x-y|, |y'-y|, |x-y'|) \geq 4 \text{ fm}, \tag{B19}$$

as defined in Eq. (27). This long-distance hadronic function is then combined with infinite volume QED weighting function for HLbL as illustrated in Fig. 8. Note that we need to sum over all permutations of x, y, y'.

APPENDIX C: SUMMAND FITTING FORM

In Sec. IV A, we have combined the disconnected diagrams and connected diagrams with a certain fraction multiplied to form $a_\mu^{\text{no-pion}}$ according to Eq. (29). We have fitted the long distance behavior of this combination with Eq. (30) and the results are shown in Fig. 6. In this appendix, we will explore other possible fitting forms and will also apply these fitting functions to other contributions.

The fitting forms are

(i) fit1: This is the form used in the main calculation, same as Eq. (29).

$$f(R_{\rm max}) = A/\text{fm}^4 \frac{R_{\rm max}^6}{R_{\rm max}^3 + (C\text{fm})^3} e^{-BR_{\rm max}/(\text{fm}\cdot\text{GeV})} \tag{C1}$$

(ii) fit2:

$$f(R_{\rm max}) = A/\text{fm}^4 R_{\rm max}^3 e^{-BR_{\rm max}/(\text{fm}\cdot\text{GeV})} \tag{C2}$$

(iii) fit3:

$$f(R_{\rm max}) = A/\text{fm} \frac{R_{\rm max}^6}{(R_{\rm max}^3 + (C\text{fm})^3)^2} e^{-BR_{\rm max}/(\text{fm}\cdot\text{GeV})} \tag{C3}$$

(iv) fit4:

$$f(R_{\rm max}) = A/\text{fm}^4 \frac{R_{\rm max}^6}{R_{\rm max}^3 + (C\text{fm})^3} e^{-m_\eta R_{\rm max}/(\text{fm}\cdot\text{GeV})} \tag{C4}$$

(v) fit5:

$$f(R_{\rm max}) = A/\text{fm}^4 R_{\rm max}^3 e^{-m_\eta R_{\rm max}/(\text{fm}\cdot\text{GeV})} \tag{C5}$$

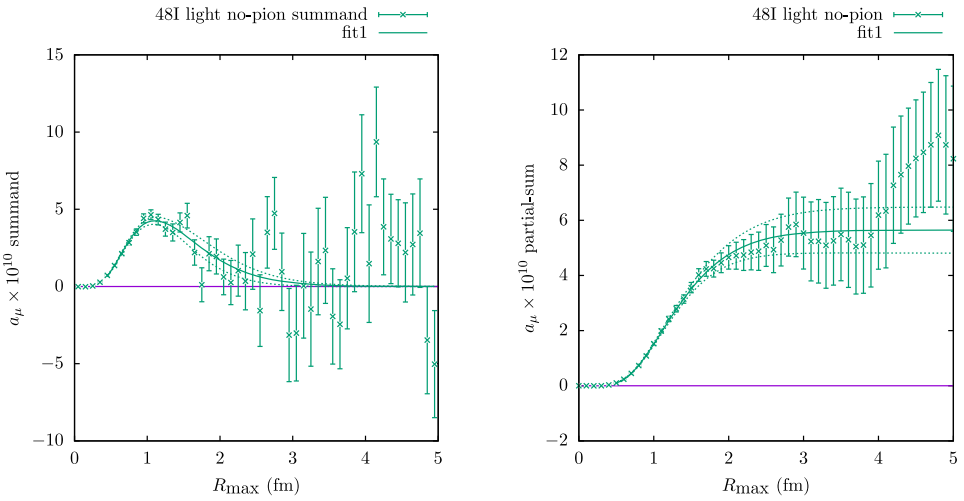

FIG. 12. Same as Fig. 6, reproduced for easy comparison with the other figures in this appendix. The fit function is Eq. (C1). The fit starts at 0.5 fm.

(vi) fit6:

$$f(R_{\max}) = A/\mathrm{fm}\frac{R_{\max}^6}{(R_{\max}^3 + (C\mathrm{fm})^3)^2} e^{-m_\eta R_{\max}/(\mathrm{fm\cdot GeV})} \tag{C6}$$

(vii) fit7:

$$f(R_{\max}) = A/\mathrm{fm}\frac{R_{\max}^6}{(R_{\max}^3 + (C\mathrm{fm})^3)^2} e^{-2m_\pi R_{\max}/(\mathrm{fm\cdot GeV})} \tag{C7}$$

(viii) fit8:

$$f(R_{\max}) = A/\mathrm{fm}\frac{R_{\max}^6}{(R_{\max}^3 + (C\mathrm{fm})^3)^2} e^{-m_\pi R_{\max}/(\mathrm{fm\cdot GeV})} \tag{C8}$$

where we set $m_\pi = 139$ MeV and $m_\eta = 550$ MeV. For "fit1," "fit2," "fit3," we always constrain the B parameter to be larger or equal to m_π.

In Figs. 12–18, we show the resulting fits along with the data.

We also apply these fit functions to different contributions, including the strange quark connected diagram, the light quark connected diagrams only, and the light quark disconnected diagrams only. Table XI summarizes the fits. The strange quark connected fits are displayed in Figs. 19–21 and, for the light quark connected diagrams, in Figs. 22–25. And finally, the light quark disconnected results are shown in Figs. 26–29. The first fit function (fit1) defined in Eq. (C1) fits the contribution from the strange quark connected diagrams, which are statistically very precise, very well. While the $\chi^2_{\mathrm{d.o.f.}}$ for this fit is quite large, this is mostly due to the small statistical error for the strange quark connected diagrams results. The difference between the fit and data for

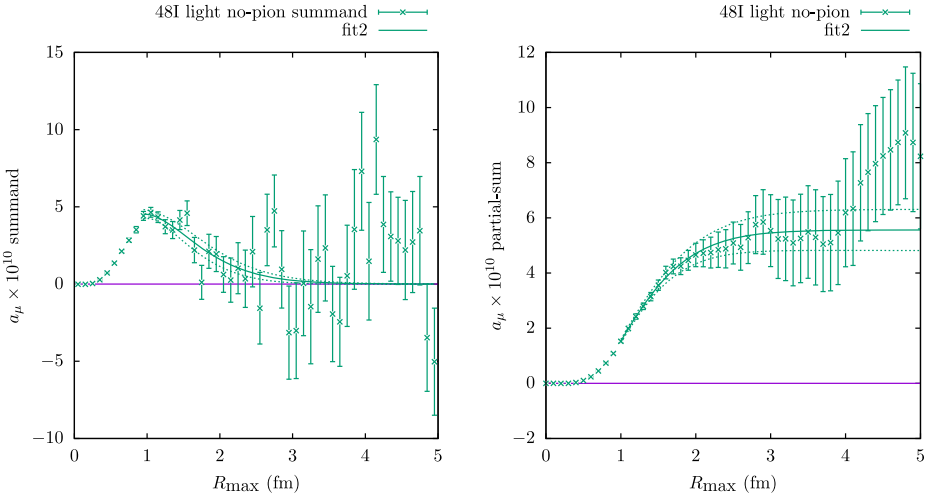

FIG. 13. Similar to Fig. 6 but with the fit function in Eq. (C2). The fit starts at 1.0 fm.

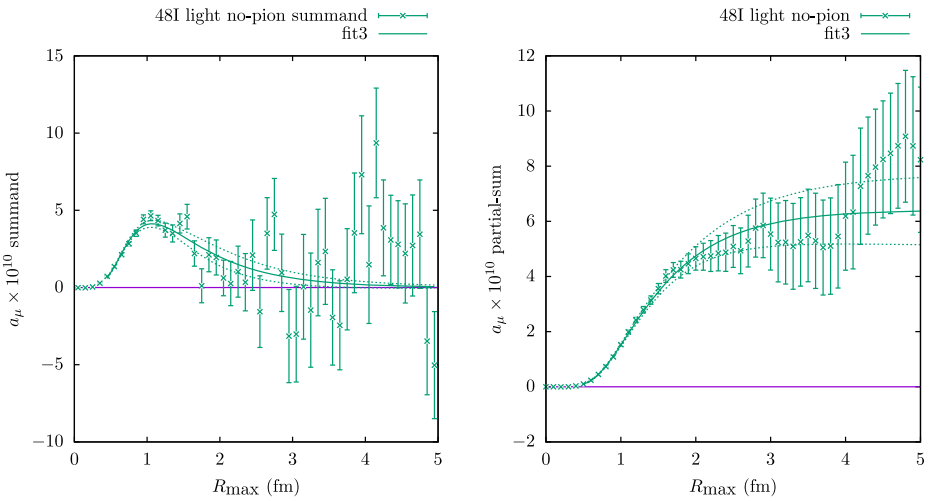

FIG. 14. Similar to Fig. 6 but with the fit function in Eq. (C3). The fit starts at 0.5 fm.

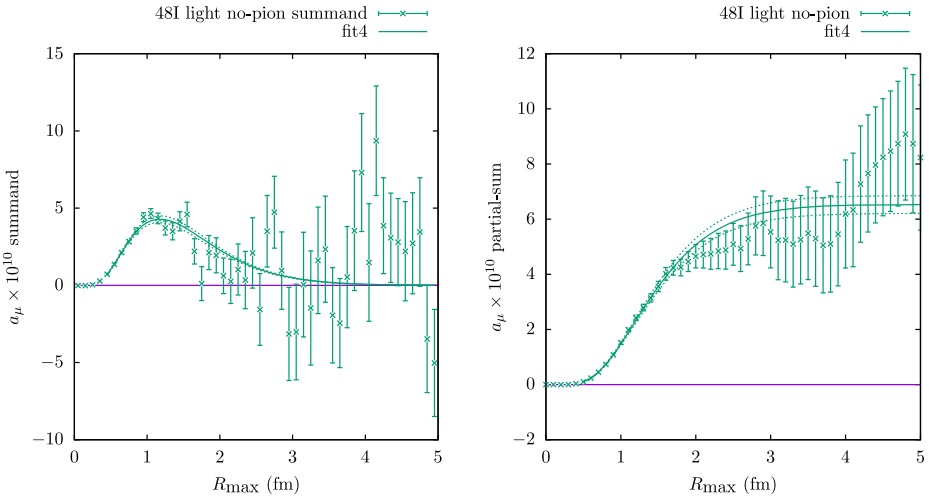

FIG. 15. Similar to Fig. 6 but with the fit function in Eq. (C4). The fit starts at 0.5 fm.

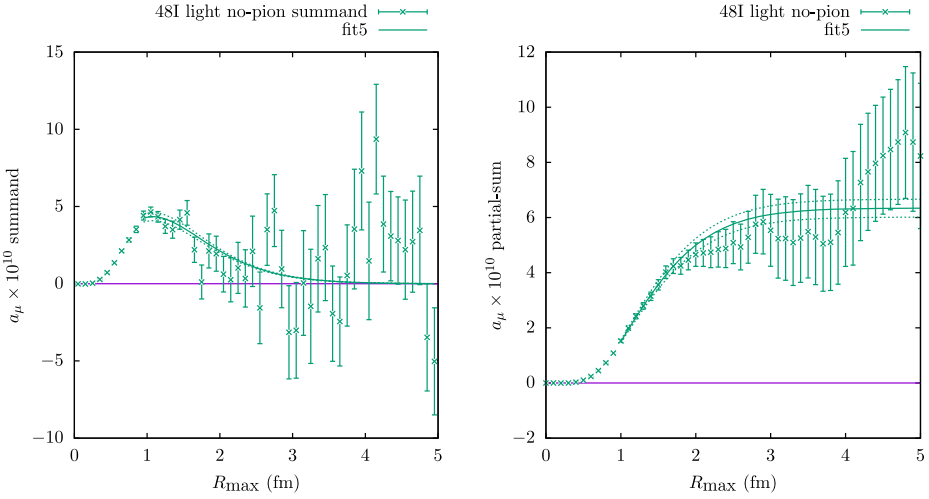

FIG. 16. Similar to Fig. 6 but with the fit function in Eq. (C5). The fit starts at 1.0 fm.

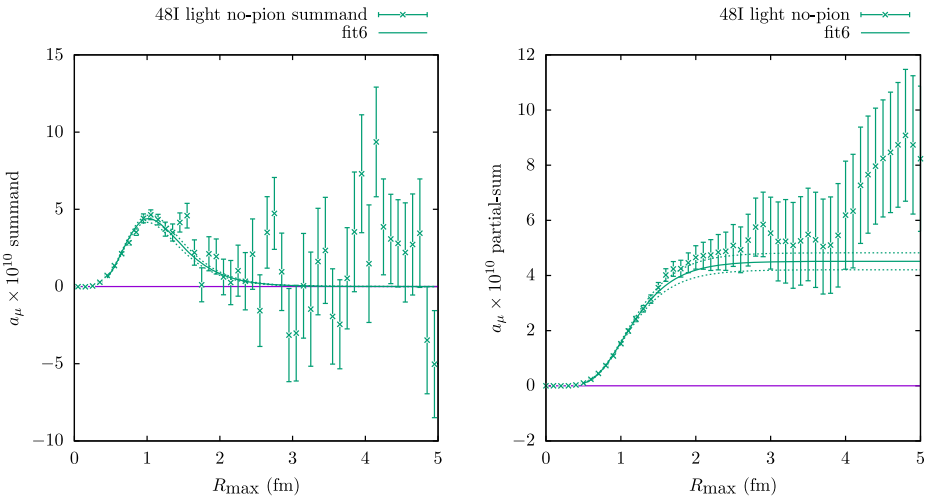

FIG. 17. Similar to Fig. 6 but with the fit function in Eq. (C6). The fit starts at 0.5 fm.

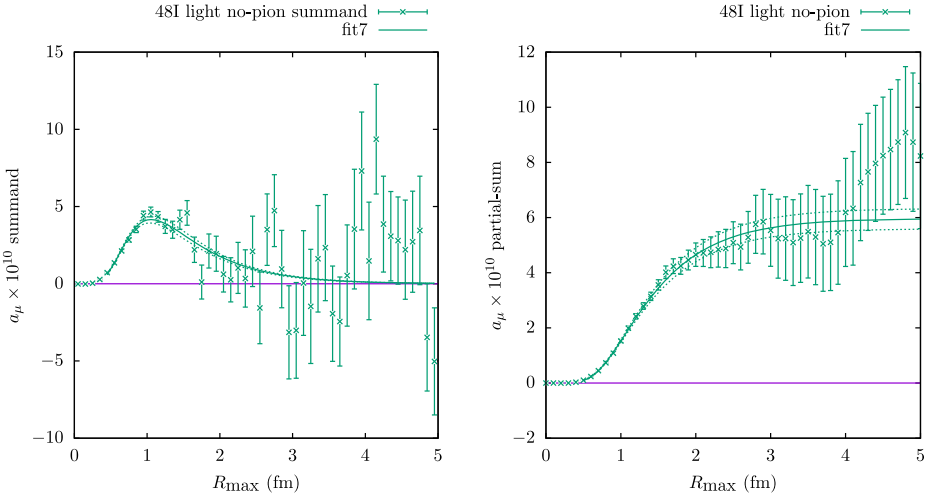

FIG. 18. Similar to Fig. 6 but with the fit function in Eq. (C7). The fit starts at 0.5 fm.

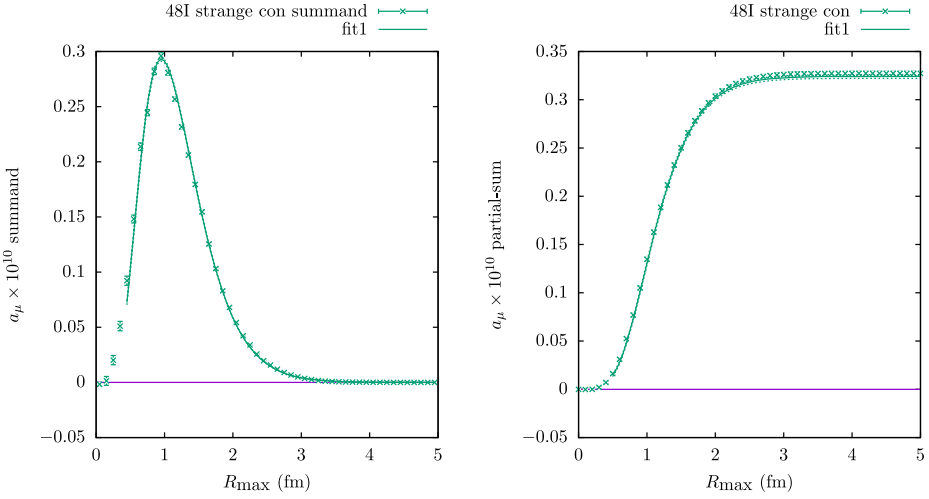

FIG. 19. Similar to Fig. 6 but for the strange quark connected contriubtion with the fit function in Eq. (C1). The fit starts at 0.5 fm.

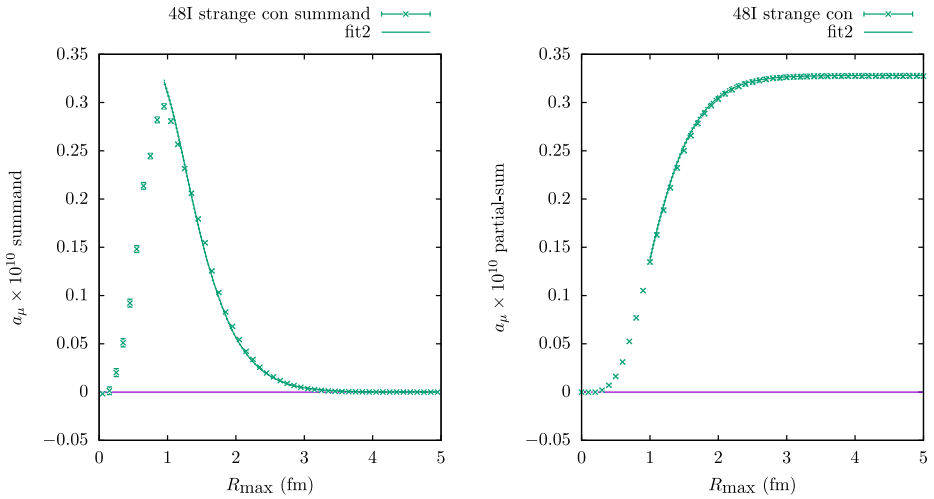

FIG. 20. Similar to Fig. 6 but for the strange quark connected contribution with the fit function in Eq. (C2). The fit starts at 1.0 fm.

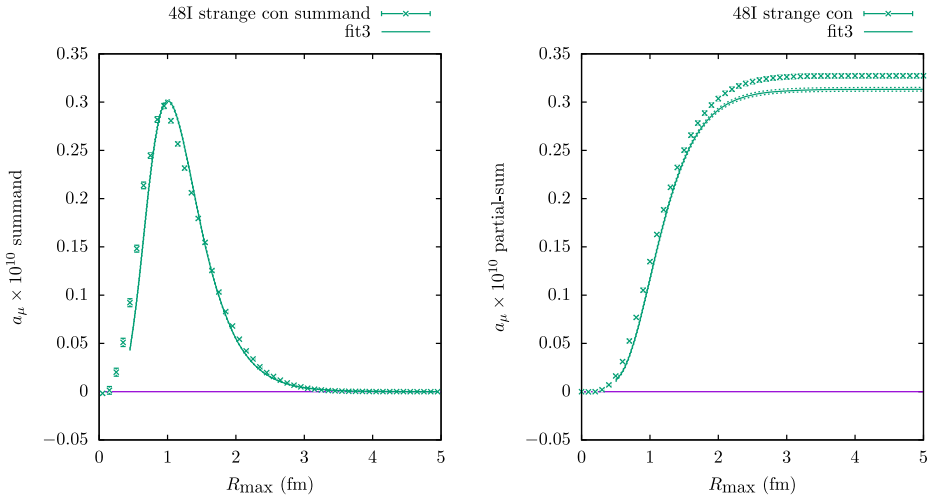

FIG. 21. Similar to Fig. 6 but for the strange quark connected contribution with the fit function in Eq. (C3). The fit starts at 0.5 fm.

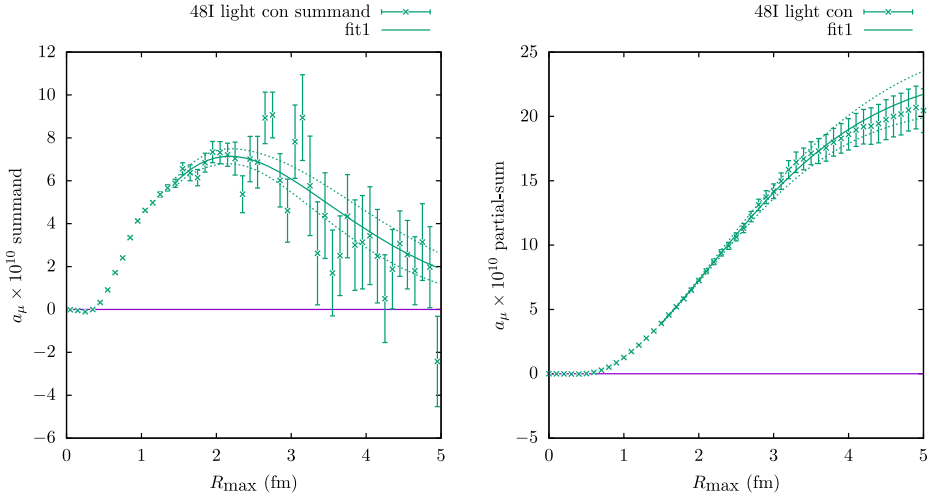

FIG. 22. Similar to Fig. 6 but for light quark connected contribution with the fit function in Eq. (C1). The fit starts at 1.5 fm.

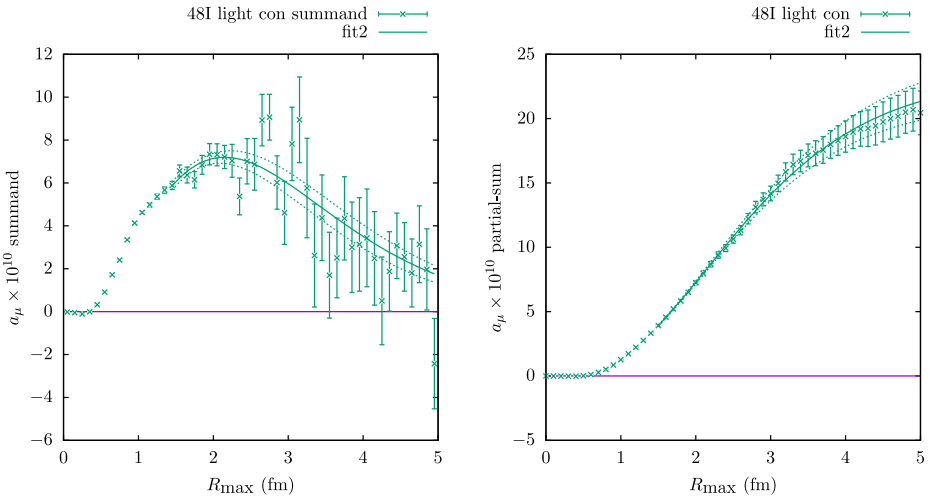

FIG. 23. Similar to Fig. 6 but for light quark connected contribution with a the fit function in Eq. (C2). The fit starts at 1.5 fm.

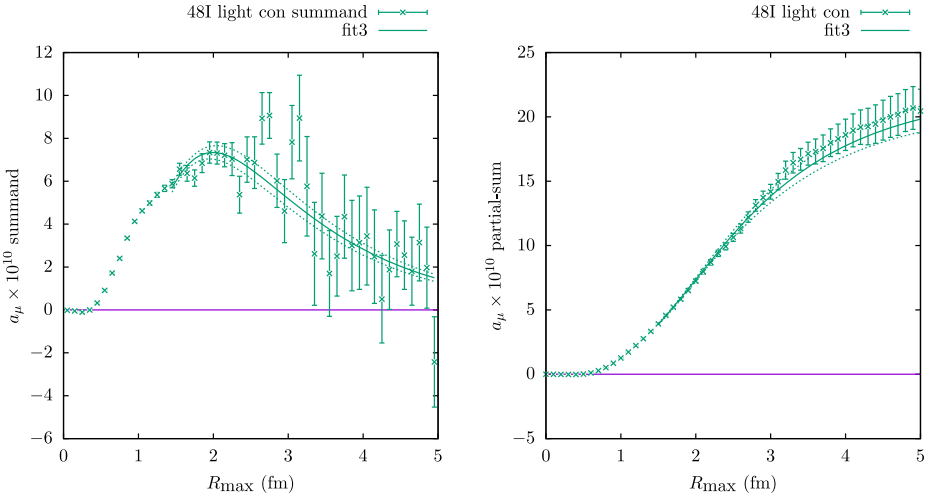

FIG. 24. Similar to Fig. 6 but for the light quark connected contribution with the fit function in Eq. (C3). The fit starts at 1.5 fm.

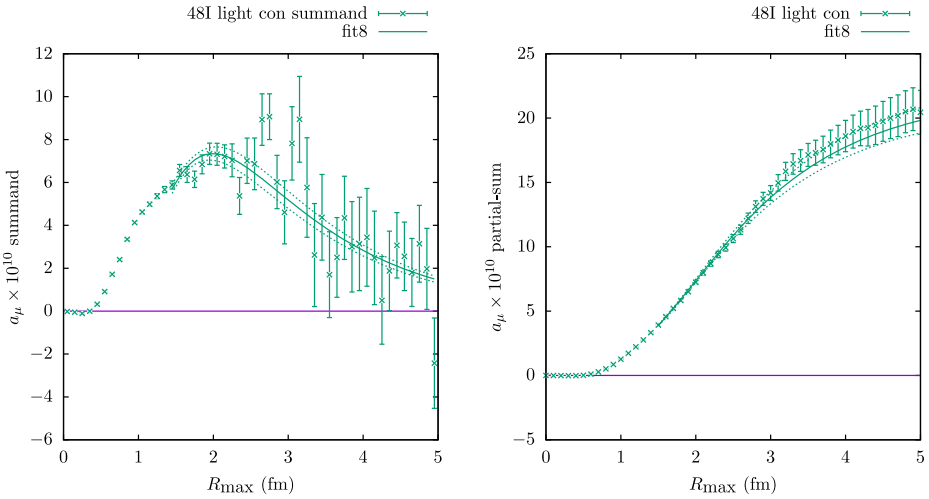

FIG. 25. Similar to Fig. 6 but for the light quark connected contribution with the fit function in Eq. (C8). The fit starts at 1.5 fm.

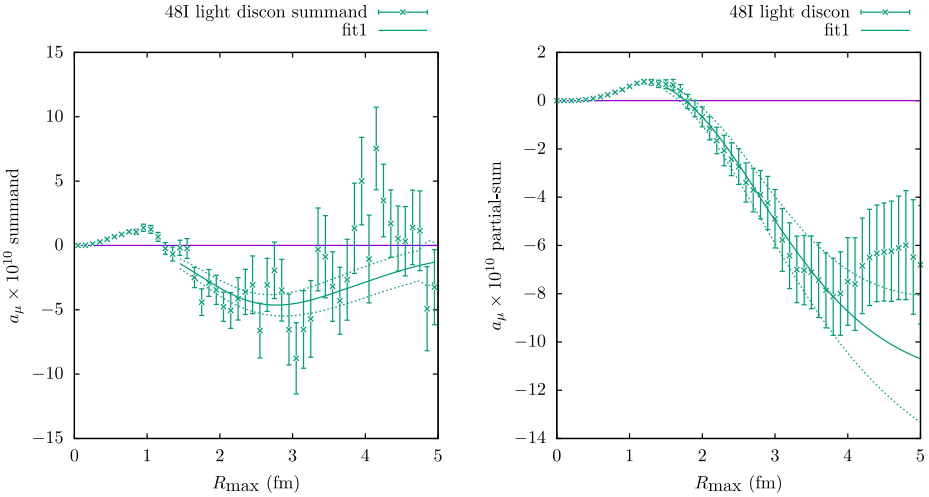

FIG. 26. Similar to Fig. 6 but for the light quark disconnected contribution with the fit function in Eq. (C1). The fit starts at 1.5 fm.

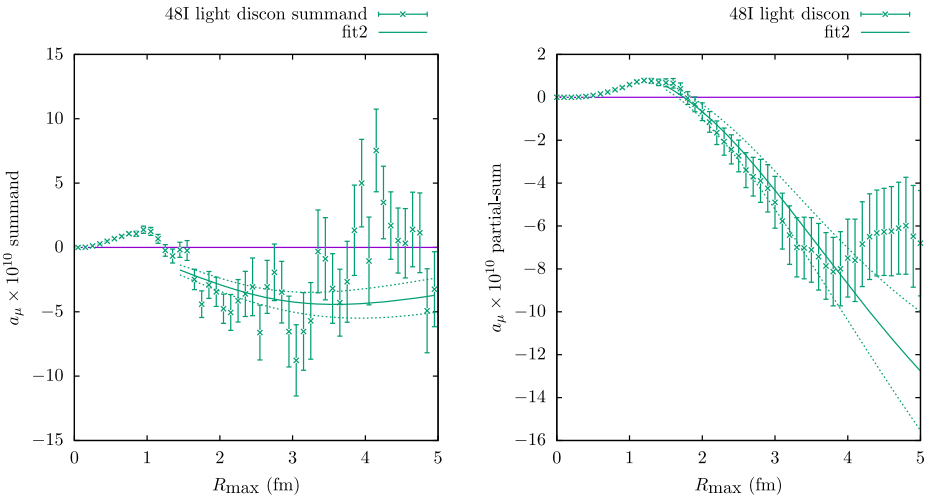

FIG. 27. Similar to Fig. 6 but for the light quark disconnected contribution with the fit function in Eq. (C2). The fit starts at 1.5 fm.

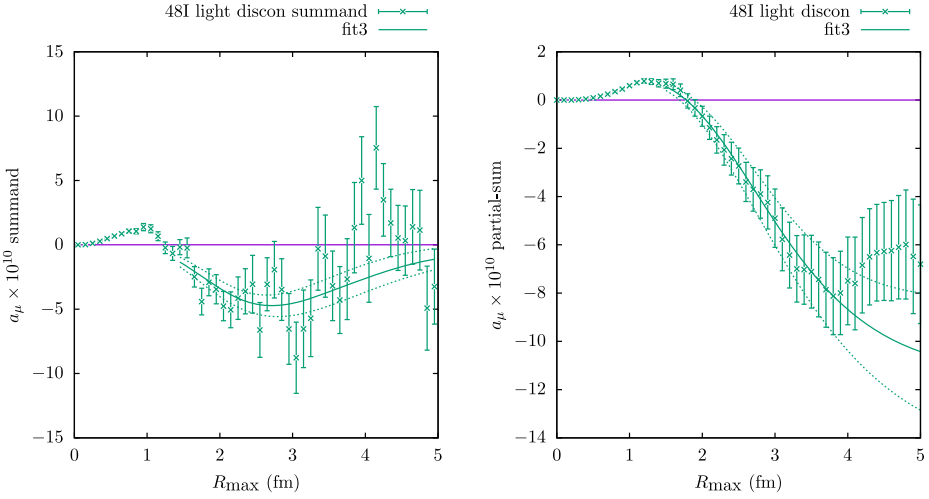

FIG. 28. Similar to Fig. 6 but for the light quark disconnected contribution with the fit function in Eq. (C3). The fit starts at 1.5 fm.

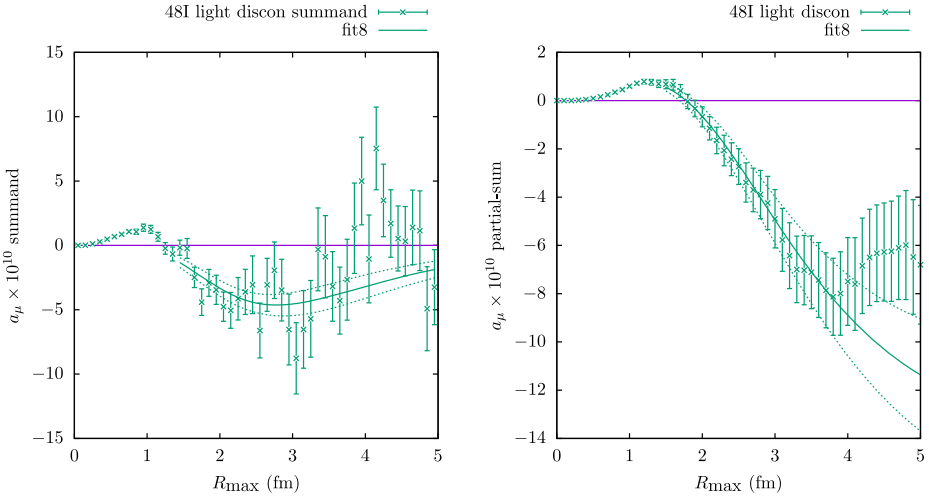

FIG. 29. Similar to Fig. 6 but for the light quark disconnected contribution with the fit function in Eq. (C8). The fit starts at 1.5 fm.

these strange quark connected diagrams results is much smaller than the needed precision for the fit for the light no-pion combinations. Based on the comparison of qualities of all the fits performed, we chose fit1 defined in Eq. (C1) as the central value for the tail part of the light quark no-pion contribution in our main calculation described in Sec. IV A.

For the light quark no-pion long-distance contributions, we observe roughly 100% variation about the central value ("fit1"), which is the reason for the 100% systematic uncertainty assigned to the contributions "48I light no-pion $R_{\max} > 2.5$ fm" and "48I light no-pion $R_{\max} > 2$ fm" in Table II. Note that the fit3 result for "48I light no-pion" has large statistical uncertainty. This is due to the fact that the data does not constrain the exponent B very much, in contrast to fit6 and fit7 which describe the data well. Since the intermediate states should have at least energy $2m_\pi$, we view the results from fit7 to be the upper bound for the fitting form fit3, which falls into the range of the results obtained with fit1 and the 100% systematic uncertainty based on the other fits.

From Table XI, we observe that the fits to the long distance parts of "48I light con" and "48I light discon" are very unreliable. Note that the statistical error for the connected diagrams and disconnected diagrams are almost

TABLE XI. The long distance part of the $a_\mu^{\text{no-pion}} \times 10^{10}$ as defined in Eq. (29) from different fits to the 48I ensemble data. The numbers in parentheses are statistical uncertainties. We perform uncorrelated fit for the summand. The minimized $\chi^2_{\text{d.o.f.}}$ is shown in the table. We also calculated the p-value using the method invented in Ref. [74], which allows a correct p-value determined for uncorrelated fits. In addition to the light no-pion contribution, we also perform the relevant fit to the data from stanage quark connected diagrams, light quark connected diagrams, and light quark disconnected diagrams. The contributions from the 48I strange quark connected diagrams are much smaller compared with other quantities. We multiply them by a factor of 1000 to fit them in this table.

Contribution name	Form	Fit range/fm	$\chi^2_{\text{d.o.f.}}$	p-value	A	B	C
48I light no-pion	Fit1	0.5–4.0	0.94	0.305	130.57748	0.62982	0.66432
48I light no-pion	Fit2	1.0–4.0	0.85	0.481	102.07658	0.61515	⋯
48I light no-pion	Fit3	0.5–4.0	1.20	0.110	25.57747	0.24408	0.70365
48I light no-pion	Fit4	0.5–4.0	1.04	0.274	76.96882	⋯	0.55112
48I light no-pion	Fit5	1.0–4.0	0.95	0.433	69.98107	⋯	⋯
48I light no-pion	Fit6	0.5–4.0	1.56	0.031	275.93065	⋯	0.98944
48I light no-pion	Fit7	0.5–4.0	1.18	0.160	32.61837	⋯	0.73081
48I strange con	Fit1	0.5–4.0	17.72	0.000	18.07733	0.76754	0.64582
48I strange con	Fit2	1.0–4.0	39.77	0.000	13.62403	0.74617	⋯
48I strange con	Fit3	0.5–4.0	79.03	0.000	15.87426	0.53922	0.94749

(Table continued)

TABLE XI. *(Continued)*

Contribution name	Form	Fit range/fm	$\chi^2_{\text{d.o.f.}}$	p-value	A	B	C
48I light con	Fit1	1.5–4.0	1.25	0.088	12.77979	0.26616	−0.59554
48I light con	Fit2	1.5–4.0	1.20	0.168	14.56237	0.27545	⋯
48I light con	Fit3	1.5–4.0	1.67	0.024	50.98630	0.13900	1.34340
48I light con	Fit8	1.5–4.0	1.60	0.042	50.98629	⋯	1.34340
48I light discon	Fit1	1.5–4.0	1.17	0.162	−43.31953	0.32417	2.85847
48I light discon	Fit2	1.5–4.0	1.48	0.060	−1.92375	0.16497	⋯
48I light discon	Fit3	1.5–4.0	1.12	0.212	−495.03384	0.22956	2.81122
48I light discon	Fit8	1.5–4.0	1.10	0.210	−72.47126	⋯	2.18553

Contribution name	Form	$R_{\text{max}} > 4$ fm	$R_{\text{max}} > 2.5$ fm	$R_{\text{max}} > 2.0$ fm
48I light no-pion	Fit1	0.01(0.02)	0.32(0.24)	0.89(0.48)
48I light no-pion	Fit2	0.01(0.02)	0.32(0.21)	0.85(0.40)
48I light no-pion	Fit3	0.15(0.27)	0.92(0.76)	1.67(1.02)
48I light no-pion	Fit4	0.03(0.00)	0.63(0.04)	1.46(0.09)
48I light no-pion	Fit5	0.03(0.00)	0.58(0.04)	1.34(0.08)
48I light no-pion	Fit6	0.00(0.00)	0.09(0.01)	0.32(0.05)
48I light no-pion	Fit7	0.08(0.01)	0.66(0.06)	1.31(0.12)
48I strange con ×1000	Fit1	0.06(0.00)	5.90(0.06)	22.72(0.15)
48I strange con ×1000	Fit2	0.08(0.00)	6.13(0.05)	22.64(0.14)
48I strange con ×1000	Fit3	0.10(0.00)	5.79(0.05)	21.40(0.14)
48I light con	Fit1	4.96(2.11)	13.14(3.04)	16.69(3.08)
48I light con	Fit2	4.43(1.06)	12.40(1.86)	15.96(2.00)
48I light con	Fit3	4.14(0.48)	11.01(1.00)	14.54(1.17)
48I light con	Fit8	4.14(0.39)	11.01(0.93)	14.54(1.12)
48I light discon	Fit1	−3.13(4.06)	−9.21(5.04)	−11.20(5.07)
48I light discon	Fit2	−13.23(6.56)	−19.61(7.61)	−21.27(7.70)
48I light discon	Fit3	−2.76(2.33)	−8.73(3.50)	−10.78(3.57)
48I light discon	Fit8	−5.22(1.84)	−11.46(3.08)	−13.46(3.24)

independent. If we fit the contributions from the connected and disconnected diagrams individually and add the results, the statistical error will approximately add up in quadrature. The difficulty of fitting the contributions from the individual connected and disconnected diagrams is likely due to the long tail from π^0 exchange. The large statistical and finite volume error in the long distance region make it hard to quantify the size of this long tail. However, combining them to form the "light no-pion" contribution with Eq. (29) cancels the long distance π^0 exchange contribution entirely, making the fit much more reliable. Still, we found some fitting form dependence even after the cancellation of the π^0 exchange contribution, which we accommodate with the 100% systematic uncertainty estimated previously.

[1] B. Abi *et al.* (Muon g-2 Collaboration), Phys. Rev. Lett. **126**, 141801 (2021).
[2] M. Abe *et al.*, Prog. Theor. Exp. Phys. **2019**, 053C02 (2019).
[3] Y. Sato (J-PARC E34 Collaboration), J. Phys. Soc. Jpn. Conf. Proc. **33**, 011110 (2021).
[4] G. Bennett *et al.* (Muon G-2 Collaboration), Phys. Rev. D **73**, 072003 (2006).
[5] T. Aoyama *et al.*, Phys. Rep. **887**, 1 (2020).
[6] T. Aoyama, M. Hayakawa, T. Kinoshita, and M. Nio, Phys. Rev. Lett. **109**, 111808 (2012).
[7] T. Aoyama, T. Kinoshita, and M. Nio, Atoms **7**, 28 (2019).
[8] A. Czarnecki, W. J. Marciano, and A. Vainshtein, Phys. Rev. D **67**, 073006 (2003); **73**, 119901(E) (2006).
[9] C. Gnendiger, D. Stöckinger, and H. Stöckinger-Kim, Phys. Rev. D **88**, 053005 (2013).
[10] M. Davier, A. Hoecker, B. Malaescu, and Z. Zhang, Eur. Phys. J. C **77**, 827 (2017).

[11] A. Keshavarzi, D. Nomura, and T. Teubner, Phys. Rev. D **97**, 114025 (2018).
[12] G. Colangelo, M. Hoferichter, and P. Stoffer, J. High Energy Phys. 02 (2019) 006.
[13] M. Hoferichter, B.-L. Hoid, and B. Kubis, J. High Energy Phys. 08 (2019) 137.
[14] M. Davier, A. Hoecker, B. Malaescu, and Z. Zhang, Eur. Phys. J. C **80**, 241 (2020); **80**, 410(E) (2020).
[15] A. Keshavarzi, D. Nomura, and T. Teubner, Phys. Rev. D **101**, 014029 (2020).
[16] A. Kurz, T. Liu, P. Marquard, and M. Steinhauser, Phys. Lett. B **734**, 144 (2014).
[17] K. Melnikov and A. Vainshtein, Phys. Rev. D **70**, 113006 (2004).
[18] P. Masjuan and P. Sanchez-Puertas, Phys. Rev. D **95**, 054026 (2017).
[19] G. Colangelo, M. Hoferichter, M. Procura, and P. Stoffer, J. High Energy Phys. 04 (2017) 161.
[20] M. Hoferichter, B.-L. Hoid, B. Kubis, S. Leupold, and S. P. Schneider, J. High Energy Phys. 10 (2018) 141.
[21] A. Gérardin, H. B. Meyer, and A. Nyffeler, Phys. Rev. D **100**, 034520 (2019).
[22] J. Bijnens, N. Hermansson-Truedsson, and A. Rodríguez-Sánchez, Phys. Lett. B **798**, 134994 (2019).
[23] G. Colangelo, F. Hagelstein, M. Hoferichter, L. Laub, and P. Stoffer, J. High Energy Phys. 03 (2020) 101.
[24] T. Blum, N. Christ, M. Hayakawa, T. Izubuchi, L. Jin, C. Jung, and C. Lehner, Phys. Rev. Lett. **124**, 132002 (2020).
[25] G. Colangelo, M. Hoferichter, A. Nyffeler, M. Passera, and P. Stoffer, Phys. Lett. B **735**, 90 (2014).
[26] J. Prades, E. de Rafael, and A. Vainshtein, Adv. Ser. Dir. High Energy Phys. **20**, 303 (2009).
[27] A. Nyffeler, Phys. Rev. D **79**, 073012 (2009).
[28] F. Jegerlehner and A. Nyffeler, Phys. Rep. **477**, 1 (2009).
[29] F. Jegerlehner, EPJ Web Conf. **166**, 00022 (2018).
[30] J. Green, O. Gryniuk, G. von Hippel, H. B. Meyer, and V. Pascalutsa, Phys. Rev. Lett. **115**, 222003 (2015).
[31] A. Gérardin, J. Green, O. Gryniuk, G. von Hippel, H. B. Meyer, V. Pascalutsa, and H. Wittig, Phys. Rev. D **98**, 074501 (2018).
[32] V. Pauk and M. Vanderhaeghen, Eur. Phys. J. C **74**, 3008 (2014).
[33] I. Danilkin and M. Vanderhaeghen, Phys. Rev. D **95**, 014019 (2017).
[34] F. Jegerlehner, *The Anomalous Magnetic Moment of the Muon* (Springer, Cham, 2017), Vol. 274.
[35] M. Knecht, S. Narison, A. Rabemananjara, and D. Rabetiarivony, Phys. Lett. B **787**, 111 (2018).
[36] G. Eichmann, C. S. Fischer, and R. Williams, Phys. Rev. D **101**, 054015 (2020).
[37] P. Roig and P. Sanchez-Puertas, Phys. Rev. D **101**, 074019 (2020).
[38] A. Gérardin, H. B. Meyer, and A. Nyffeler, Phys. Rev. D **94**, 074507 (2016).
[39] C. Alexandrou *et al.*, Phys. Rev. D **108**, 054509 (2023).
[40] S. Burri *et al.*, Proc. Sci. LATTICE2022 (**2023**) 306 [arXiv:2212.10300].
[41] T. Blum, S. Chowdhury, M. Hayakawa, and T. Izubuchi, Phys. Rev. Lett. **114**, 012001 (2015).
[42] T. Blum, N. Christ, M. Hayakawa, T. Izubuchi, L. Jin, and C. Lehner, Phys. Rev. D **93**, 014503 (2016).
[43] T. Blum, N. Christ, M. Hayakawa, T. Izubuchi, L. Jin, C. Jung, and C. Lehner, Phys. Rev. Lett. **118**, 022005 (2017).
[44] M. Hayakawa and S. Uno, Prog. Theor. Phys. **120**, 413 (2008).
[45] N. Asmussen, J. Green, H. B. Meyer, and A. Nyffeler, Proc. Sci. LATTICE2016 (**2016**) 164 [arXiv:1609.08454].
[46] T. Blum, N. Christ, M. Hayakawa, T. Izubuchi, L. Jin, C. Jung, and C. Lehner, Phys. Rev. D **96**, 034515 (2017).
[47] E.-H. Chao, A. Gérardin, J. R. Green, R. J. Hudspith, and H. B. Meyer, Eur. Phys. J. C **80**, 869 (2020).
[48] E.-H. Chao, R. J. Hudspith, A. Gérardin, J. R. Green, H. B. Meyer, and K. Ottnad, Eur. Phys. J. C **81**, 651 (2021).
[49] E.-H. Chao, R. J. Hudspith, A. Gérardin, J. R. Green, and H. B. Meyer, Eur. Phys. J. C **82**, 664 (2022).
[50] S. Laporta and E. Remiddi, Phys. Lett. B **301**, 440 (1993).
[51] S. Laporta and E. Remiddi, Phys. Lett. B **265**, 182 (1991).
[52] T. Blum *et al.* (RBC, UKQCD Collaborations), Phys. Rev. D **93**, 074505 (2016).
[53] D. Renfrew, T. Blum, N. Christ, R. Mawhinney, and P. Vranas, Proc. Sci. LATTICE2008 (**2008**) 048 [arXiv:0902.2587].
[54] M. Abramczyk, S. Aoki, T. Blum, T. Izubuchi, H. Ohki, and S. Syritsyn, Phys. Rev. D **96**, 014501 (2017).
[55] T. Blum, P. A. Boyle, V. Gülpers, T. Izubuchi, L. Jin, C. Jung, A. Jüttner, C. Lehner, A. Portelli, and J. T. Tsang (RBC, UKQCD Collaborations), Phys. Rev. Lett. **121**, 022003 (2018).
[56] T. Blum *et al.*, arXiv:2301.08696.
[57] M. A. Clark, C. Jung, and C. Lehner, in *35th International Symposium on Lattice Field Theory (Lattice 2017) Granada, Spain, 2017* (2017), arXiv:1710.06884.
[58] T. Blum, T. Izubuchi, and E. Shintani, Phys. Rev. D **88**, 094503 (2013).
[59] W. Detmold, D. J. Murphy, A. V. Pochinsky, M. J. Savage, P. E. Shanahan, and M. L. Wagman, Phys. Rev. D **104**, 034502 (2021).
[60] Y. Li, S.-C. Xia, X. Feng, L.-C. Jin, and C. Liu, Phys. Rev. D **103**, 014514 (2021).
[61] J. Bijnens and J. Relefors, J. High Energy Phys. 09 (2016) 113.
[62] L. Jin, T. Blum, N. Christ, M. Hayakawa, T. Izubuchi, C. Jung, and C. Lehner, Proc. Sci. LATTICE2016 (**2016**) 181 [arXiv:1611.08685].
[63] One can use different setup for the connected and disconnected diagrams, in which case this relation will not hold exactly. For example, Ref. [48] uses different setups.
[64] Y. Zhao, Lattice calculation of the $\pi^0 \to e^+e^-$ and the $K_L \to \gamma\gamma$ decays, Ph.D. thesis, Columbia University, 2022.
[65] N. Asmussen, E.-H. Chao, A. Gérardin, J. R. Green, R. J. Hudspith, H. B. Meyer, and A. Nyffeler, J. High Energy Phys. 04 (2023) 040.
[66] X. Feng, S. Aoki, H. Fukaya, S. Hashimoto, T. Kaneko, J.-i. Noaki, and E. Shintani, Phys. Rev. Lett. **109**, 182001 (2012).
[67] B. Moussallam, Phys. Rev. D **51**, 4939 (1995).
[68] M. Knecht, S. Peris, M. Perrottet, and E. de Rafael, Phys. Rev. Lett. **83**, 5230 (1999).

[69] M. J. Ramsey-Musolf and M. B. Wise, Phys. Rev. Lett. **89**, 041601 (2002).
[70] T. Kinoshita, B. Nizic, and Y. Okamoto, Phys. Rev. D **31**, 2108 (1985).
[71] M. Hayakawa, T. Kinoshita, and A. I. Sanda, Phys. Rev. Lett. **75**, 790 (1995).
[72] J. Bijnens, EPJ Web Conf. **118**, 01002 (2016).
[73] N. Christ, X. Feng, L. Jin, C. Tu, and Y. Zhao, Phys. Rev. Lett. **130**, 191901 (2023).
[74] N. Christ, R. Eranki, and C. Kelly (RBC, UKQCD Collaboration), arXiv:2409.11379.